



Long-lived magmatic evolution and mineralization resulted in formation of the giant Cuonadong Sn-W-Be polymetallic deposit, southern Tibet

Zuowen Dai ^{a,b}, Guangming Li ^{b,*}, Zhiming Yang ^{a,c,*}, Yuling Xie ^a, Jiangang Fu ^b, Anping Xiang ^b, Jan Marten Huizenga ^{d,e,f}, Chunmei Huang ^b, Wei Liang ^b, Huawei Cao ^b

^a School of Civil and Resource Engineering, University of Science and Technology Beijing, Beijing 100083, China

^b Chengdu Center, China Geological Survey, Chengdu 610081, China

^c Institute of Geology, Chinese Academy of Geological Sciences, Beijing 100037, China

^d Faculty of Environmental Sciences and Natural Resource Management, Norwegian University of Life Sciences, P.O. Box 5003, NO-1432 Ås, Norway

^e Economic Geology Research Centre (EGRU), James Cook University, Townsville 4811, Australia

^f Department of Geology, University of Johannesburg, PO Box 524, Auckland Park 2006, South Africa



ARTICLE INFO

Keywords:

Leucogranite
Fractional crystallization
Sn-W-Be deposit
Supernormal enrichment
Cuonadong
Himalaya

ABSTRACT

The Cuonadong Sn-W-Be polymetallic deposit is the first Cenozoic leucogranite-related rare-metal deposit with giant metallogenic potential in the Himalayan orogen. However, the controlling factors for the supernormal enrichment of beryllium, tin and tungsten in this deposit remain vague. In this study, we carried out systematic geochronological, whole-rock geochemical, and Sr-Nd isotopic analysis for the Cuonadong leucogranites, as well as detailed ore-forming geochronological study for the rare-metal mineralization. The monazite U-Th-Pb, cassiterite U-Pb and muscovite Ar-Ar dating results, together with previously reported geochronological data, indicate that the major Cuonadong leucogranites (including, from old to young, the weakly-oriented two-mica granite, two-mica granite and the muscovite granite) were formed during ~ 21–15 Ma, whereas the Sn-W-Be mineralization mainly occurred at ~ 18–14 Ma. The Cuonadong leucogranites show strong peraluminous ($A/CNK = 1.09\text{--}1.22$) features, and have high SiO_2 (71.62–75.97 wt%) and Al_2O_3 (14.04–16.09 wt%) and low MgO (0.07–0.33 wt%), MnO (0.01–0.15 wt%) and total iron ($\text{Fe}_2\text{O}_3^T = 0.36\text{--}1.01$ wt%) contents, and are enriched in large ion lithophile elements (e.g., Rb, U, K, and Pb). These geochemical features, together with enriched Sr-Nd isotopes ($\epsilon\text{Nd(t)} = -15.7$ to -11.7 ; $(^{87}\text{Sr}/^{86}\text{Sr})_i = 0.71957\text{--}0.76313$), indicate that the Cuonadong leucogranites belong to S-type granite and were derived from muscovite-induced dehydration melting of metapelites of the Higher Himalayan Crystalline Sequence. Perceptible linear variations of some major elements (e.g., Na_2O , K_2O , MnO , Fe_2O_3^T , TiO_2 and A/CNK) with increasing Rb/Sr ratios suggest that these leucogranites experienced different degrees of evolution. Quantitative simulation calculations based on the whole-rock Rb, Sr, and Ba contents imply that the Cuonadong leucogranites experienced increasingly-strong fractional crystallization of plagioclase, K-feldspar and biotite from the weakly-oriented two-mica granite through the two-mica granite to the muscovite granite. Importantly, intense fractional crystallization led to notable enrichment of Sn, W and Be, although these elements are not obviously high in the relatively primitive magma for the Cuonadong leucogranites. Significantly, evident REE tetrad effects and deviation of twin-element pair ratios (e.g. K/Rb , K/Ba , Zr/Hf , Nb/Ta , and Y/Ho) from the chondritic values demonstrate that intense interaction between melts and volatile-rich aqueous fluids occurred during magmatic evolution. This implies that the Cuonadong leucogranites were derived from a volatile-rich magmatic system. The abundant volatiles probably facilitated occurrence of fractional crystallization and extended duration of this process through lowering the solidus and viscosity of the magma. Thus, we propose that the long-lived fractional crystallization (21–15 Ma) and rare-metal mineralization (18–14 Ma) collectively led to supernormal enrichment of Sn, W, and Be in the Cuonadong Sn-W-Be polymetallic deposit. In contrast, the enrichment of these rare-metal elements was insignificant during partial melting.

* Corresponding authors at: Chengdu Center, China Geological Survey, Jinniu District, Chengdu 610081, Sichuan Province, China (G.-M. Li). Institute of Geology, Chinese Academy of Geological Sciences, Xicheng District, Beijing 100037, China (Z.-M. Yang).

E-mail addresses: 13982257109@163.com (G. Li), zm.yang@hotmail.com (Z. Yang).

1. Introduction

Since the closure of the Neo-Tethys Ocean and subsequent collision between India and Eurasia in the Early Cenozoic (55 ± 10 Ma; Mo et al., 2007; Zhu et al., 2015), the Himalayan orogen has experienced notable crustal thickening and extensive anatexis (Harris and Massey, 1994; Patiño Douce and Harris, 1998; Zeng et al., 2011; Hou et al., 2012; Dai et al., 2020; Cao et al., 2021a), which triggered formation of the world-renowned Himalayan leucogranite belt (Wu et al., 2015, 2020). The Himalayan leucogranites were traditionally considered as products of in situ anatexis of the Higher Himalayan Crystalline Sequence in the late metamorphic stage (Le Fort et al., 1987). Normally, this type of rock is less associated with rare-metal mineralization. Thus, the importance of rare-metal mineralization in the Himalaya was never been highly considered. However, recent studies showed that the Himalayan leucogranites are highly fractionated peraluminous granites with rare-metal mineralization potential (Wang et al., 2017, 2020; Cao et al., 2022a). This is supported by successive discovery of a few rare-metal deposits/occurrences, such as Cuonadong Sn-W-Be polymetallic deposit (Li et al., 2017a), Gabo lithium deposit (Li et al., 2022), Lalong rare-metal polymetallic deposit (Huang et al., 2019), Qongjiagang lithium deposit (Qin et al., 2021), and several other rare-metal mineralization occurrences (Zhang et al., 2022). Thus, the Himalaya is expected to be a

new promising rare-metal metallogenic belt (Wu et al., 2020; Cao et al., 2022b).

It is noteworthy that among these newly-discovered deposits the Cuonadong Sn-W-Be polymetallic deposit is the first rare-metal deposit with giant metallogenetic potential in the Himalayan orogen (Li et al., 2017a; Cao et al., 2021b; Dai et al., 2022). A series of previous studies have shown that this deposit is genetically related to the Cenozoic leucogranites within ore district based on geological survey, rock- and ore-forming geochronological and C-H-O-S-Pb-Sr isotopic data (Liang et al., 2018; Cao et al., 2020, 2021b; Xie et al., 2020; Dai et al., 2022). According to early estimate, only in Xianglin (one of the four areas with intensive and intense rare-metal mineralization in this deposit) the inferred Sn resources are up to 80,000 t (@ 0.36%); WO₃ resources are up to 50,000 t (@ 0.21%); and BeO resources are up to 34,000 t (@ 0.08%) based on preliminary exploration (Li et al., 2017a). However, the governing factors for supernormal enrichment of beryllium, tin and tungsten in the Cuonadong deposit is still unclear. This knowledge gap hinders our comprehensive understanding of the rare-metal metallogeny in the Himalayan orogen, and will probably limit our future prospecting breakthroughs. Hence, it is urgent to address this issue.

In this study, we carried out systematic geochronological, whole-rock geochemical, and Sr-Nd isotopic analysis for the Cuonadong leucogranites, together with metallogenic geochronological studies for the

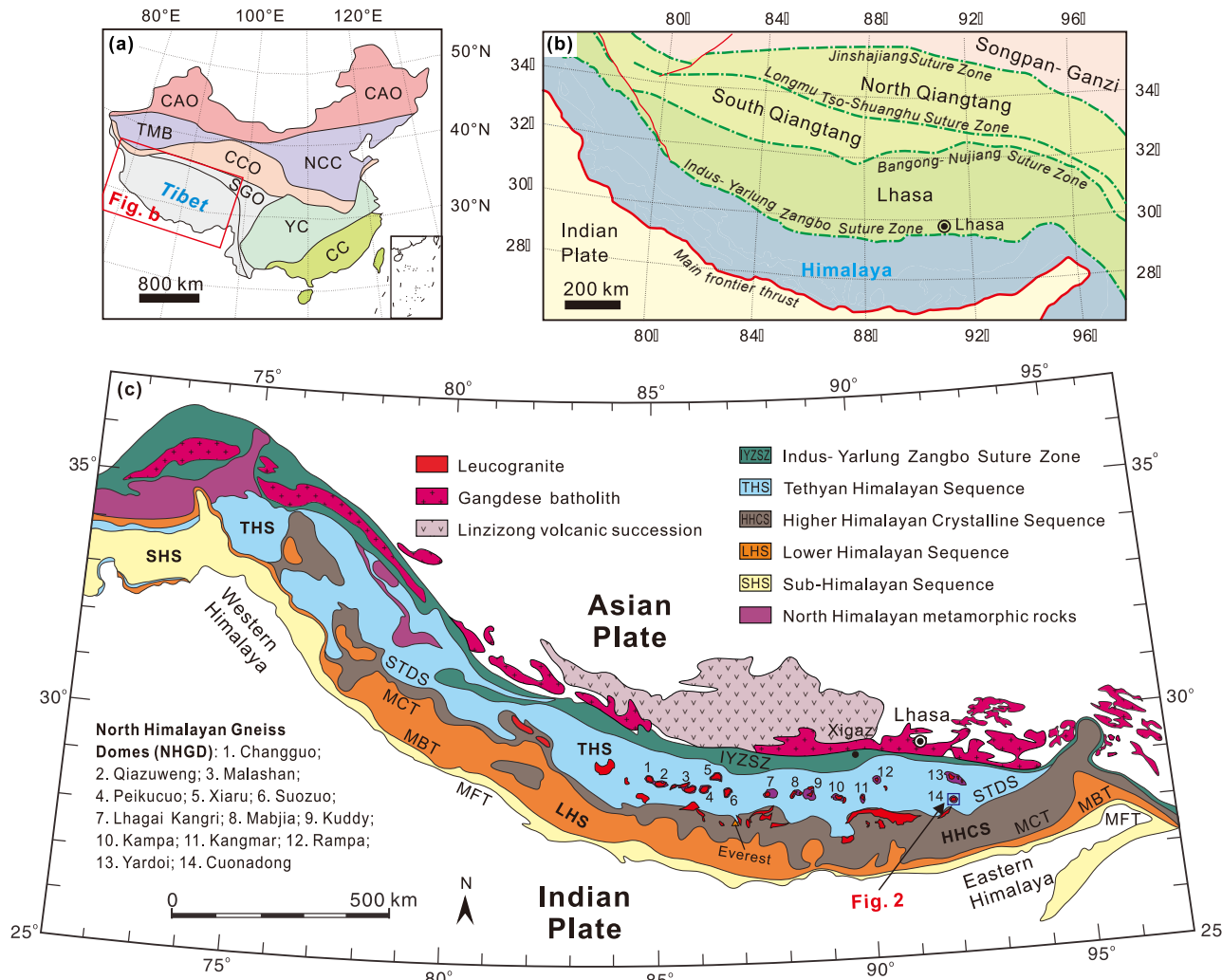


Fig. 1. (a) Tectonic map of China, showing the location of Tibet (modified after Pan et al., 2009). (b) Tectonic subdivision of the Tibet Plateau, showing the major sutures and terranes (modified after Yin and Harrison, 2000; Pan et al., 2012). (c) Simplified geological map of Himalaya showing the subdivision of Himalaya and distribution of Himalayan leucogranites (modified after Zhang et al., 2012; Wu et al., 2020; Pan et al., 2012). CAO: Central Asia Orogen; TMB: Tarim Block; NCC: North China Craton; CCO: Central China Orogen; SGO: Songpan Ganzi Orogen; YC: Yangtza Craton; CC: Cathaysia Craton.

Cuonadong Sn-W-Be deposit. Using the results of this study and previously published data, we investigated the controlling mechanisms for the supernormal enrichment of ore-forming elements in the Cuonadong, from the aspect of magma generation, evolution and rare-metal mineralization. Finally, we proposed that the long-lived magmatic evolution and rare-metal mineralization process collectively facilitated the formation of the giant Cuonadong Sn-W-Be polymetallic deposit.

2. Geological setting

The Tibetan Plateau orogen, located in west of China (Fig. 1a; Pan et al., 2009), is a tectonic collage of five east–west trending terranes. It includes (from north to south) the Songpan-Ganzi, North Qiangtang (also known as East Qiangtang), South Qiangtang (also known as West Qiangtang), Lhasa, and Himalaya. These terranes are bounded by Jinshajiang, Longmu Tso-Shuanghu, Bangong-Nujiang and Indus-Yarlung-Zangbo suture zones, respectively (Fig. 1b; Yin and Harrison, 2000; Pan et al., 2012).

The Himalayan orogenic belt is an intensely deformed magmatic-metamorphic belt formed during the Cenozoic India-Eurasia collision (Fig. 1c; Yin and Harrison, 2000; Pan et al., 2012). It is separated from the Indian plate to the south by the Main Frontier Thrust and from the Lhasa terrane in the north by the Indus-Yarlung Zangbo suture zone. The Himalayan orogenic belt is subdivided into the Tethyan Himalaya, the Higher Himalaya, the Lower Himalaya, and the Sub-Himalaya, which are separated from each other by the south Tibet detachment system, the Main Central Thrust, and the Main Boundary Thrust, respectively (Fig. 1c; Yin and Harrison, 2000; Yin, 2006). The Tethyan Himalaya Sequence comprises Paleozoic to Paleogene low-grade metamorphic or unmetamorphosed siliciclastic and carbonate rocks (Myrow et al., 2019), which were deposited on the Indian passive continental margin (Cao et al., 2018). The Higher Himalayan Crystalline Sequence comprises Late Proterozoic to Early Paleozoic upper amphibolite- to lower granulite-facies metamorphic rocks (Kohn, 2014; Mukherjee et al., 2019). The Lower Himalayan Sequence consists of Proterozoic greenschist to amphibolite facies metasedimentary rocks (Kohn, 2014). The Sub-Himalayan Sequence consists of Neogene alluvial sedimentary rocks that represent an overfilled stage of the Himalayan foreland basin.

Two sub-parallel leucogranite belts, namely the Tethyan Himalayan leucogranite belt (also referred to as the North Himalayan leucogranite belt) to the north and the Higher Himalayan leucogranite belt to the south, occur in the Himalayan area (Fig. 1c; Zhang et al., 2012; Wu et al., 2020; Cao et al., 2022b). The vast majority of the Tethyan Himalayan leucogranites are exposed in the cores of the north Himalayan gneiss domes, except for a few isolated intrusive bodies that intruded into the Tethyan Himalayan Sequence (such as the Dala and Quedang two-mica granites) (Fig. 1c; Zhang et al., 2012; Wu et al., 2020; Cao et al., 2022b). The Higher Himalayan leucogranites, on the other hand, were emplaced into the Higher Himalayan Crystalline Sequence adjacent to the South Tibetan detachment system, forming a discontinuous chain of sheets, dykes, sills, and laccolithic bodies (Fig. 1c; Zhang et al., 2012; Wu et al., 2020; Cao et al., 2022b). The Himalayan leucogranites comprise biotite granite, two-mica granite, muscovite granite, tourmaline granite, and garnet granite. These leucogranites were emplaced between 48.5 and 6.8 Ma (Cao et al., 2022b). The Eocene leucogranites are characterized by high Sr/Y ratios, thus are considered as products of partial melting of a thickened lower crust comprising amphibolite with subordinate metapelites (Zeng et al., 2011; Hou et al., 2012; Dai et al., 2020). The Miocene leucogranites are considered as highly fractionated crust-derived peraluminous S-type granites (Wu et al., 2015, 2020; Hopkinson et al., 2017) and have great potential for rare-metal mineralization (Li et al., 2017a; Wang et al., 2017; Huang et al., 2019; Wu et al., 2020; Cao et al., 2022b; Li et al., 2022; Zhang et al., 2022).

The Cuonadong Sn-W-Be polymetallic deposit occurs in the Cuonadong gneiss dome, eastern segment of the Tethyan Himalaya (Fig. 1c; Fu et al., 2017; Li et al., 2017a). The Cuonadong gneiss dome is a newly-

identified dome with an exposed area of about 400 km² (Fig. 2; Fu et al., 2017). The dome comprises three lithological-tectonic units, i.e. the lower-located core, the mantle in the center, and the upper-located rim, which are separated from each other by a ductile lower detachment fault and a brittle upper detachment fault (Fig. 2, 3a-c; Fu et al., 2017). The core comprises Early Paleozoic augen orthogneiss (ca. 500 Ma; Zhang et al., 2019a), minor Neoproterozoic granitic gneiss (825–820 Ma; Zhang et al., 2021), migmatite, amphibolite (ca. 826 Ma; Zhang et al., 2021) and paragneiss (Figs. 2, 3b). The mantle comprises strongly deformed schist, marble, subordinate amphibolite and quartzite (Fig. 2, 3b-d). The rim consists of Jurassic and minor Triassic low-grade meta-sedimentary rocks and sedimentary rocks that belong to the Tethyan Himalayan Sequence, including silty mudstone, siltstone, slate, and minor phyllite (Fig. 2; Fu et al., 2017).

It is noteworthy that voluminous leucogranites/pegmatites were intruded into the dome, particularly in the core and mantle of the dome (Fig. 2), including: (1) strongly-deformed two-mica granite/pegmatite, normally exposed in the mantle of the dome and occurs in the shape of lenticle, boudin or tight/sheath fold (Figs. 2 and 3d; Fu et al., 2020; Zhang et al., 2020); (2) weakly-oriented two-mica granite, mainly exposed in northern part of the dome (Figs. 2, 3e); (3) two-mica granite, mainly exposed in center and southwestern part of the dome (Figs. 2, 3f); (4) muscovite granite, mainly exposed in eastern part of the dome (Figs. 2, 3e-g); and (5) pegmatite (pegmatite in the following text refers to such type unless specified) (Figs. 2, 3g-h). The latter four rock types constitute the main part of the Cuonadong intrusion (Fig. 2). The weakly-oriented two-mica granite is medium- to fine-grained and comprises quartz (30–35 vol%), K-feldspar (25–30 vol%), plagioclase (25–30 vol%), biotite (8–10 vol%), and muscovite (8–10 vol%) with accessory apatite, monazite and zircon (Fig. 4a, d). The two-mica granite is fine-grained and comprises quartz (30–35 vol%), K-feldspar (20–25 vol%), plagioclase (30–35 vol%), muscovite (10–15 vol%), biotite (5–8 vol%) and minor garnet (locally), with accessory tourmaline, apatite, monazite, zircon, and columbite (Fig. 4b, e). The muscovite granite is fine-grained and comprises quartz (30–35 vol%), plagioclase (30–35 vol%), K-feldspar (10–15 vol%), muscovite (15–20 vol%), garnet (3–8 vol%) and tourmaline (1–5 vol%), with accessory beryl, monazite, zircon and columbite (Fig. 4c, f). The pegmatite contains plagioclase, quartz, and muscovite, with variable amounts of beryl, tourmaline, and garnet, and accessory zircon, monazite and columbite (Fig. 3g-h).

Four areas with intensive and intense rare-metal mineralization were identified in the Cuonadong dome, including the Xianglin (Zabulu), Yunazha, Rina and Changming (Fig. 2; Cao et al., 2020, 2021b; Dai et al., 2022). Within these areas, four major types of rare-metal mineralization were identified, including: (1) pegmatite-type Be mineralization, which developed in beryl-rich pegmatite (Fig. 3 h); (2) greisen-type Sn mineralization, which normally occurs as greisen veins developed in muscovite granite/pegmatite and are composed mainly of quartz, muscovite, cassiterite and tourmaline (Fig. 5a, d); (3) skarn-type W-Sn-Be mineralization (Fig. 5b, e), which mainly occurs at the contact zone between the muscovite granite/pegmatite and the marble in the mantle of the Cuonadong dome (Fig. 5b); (4) hydrothermal vein-type Sn-W-Be-F mineralization (Fig. 5c, f), which normally occurs in NE-striking faults that cut the gneiss, marble, skarn, leucogranite, and pegmatite (Figs. 2, 5c). Spatially, these ore/mineralized bodies show close correlation to the Cuonadong leucogranites, especially the muscovite granite/pegmatite (Figs. 3 h, 5a-c).

3. Samples and analytical methods

In this study, the weakly-oriented two-mica granite, two-mica granite and the muscovite granite were selected as the main objects for geochronological, Sr-Nd isotopic and whole-rock compositional research considering their huge volume and close spatial relationship to the rare-metal mineralization. This is combined with ore-forming geochronological study. In detail, two granite samples (one weakly-

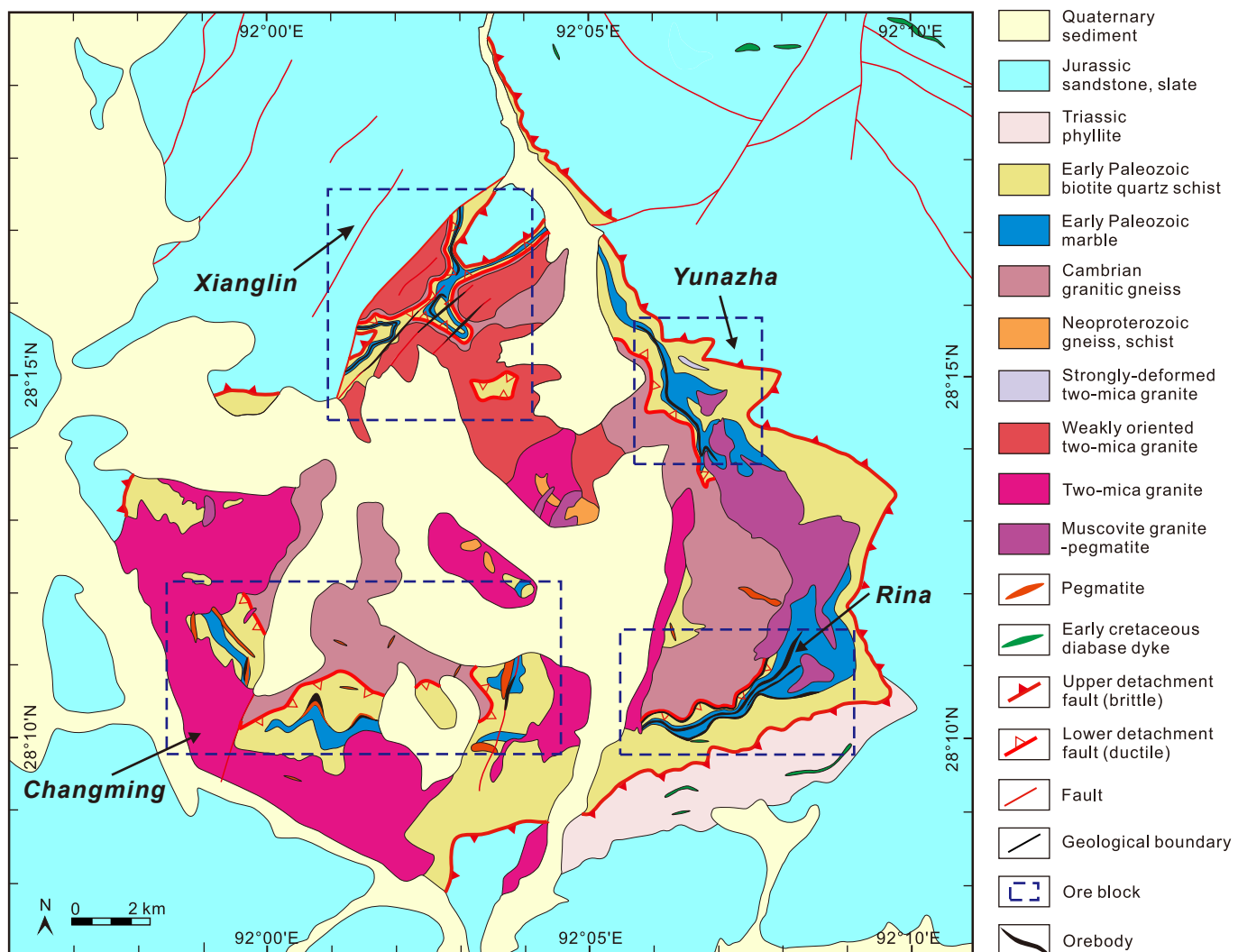


Fig. 2. Simplified geological map of the Cuonadong gneiss dome (modified after Dai et al., 2022).

oriented two-mica granite sample and one unoriented two-mica granite sample) were used for in situ LA-ICP-MS monazite U-Th-Pb dating, one beryl-rich pegmatite sample was used for bulk muscovite Ar-Ar dating, four cassiterite-bearing ores (three greisen samples and one skarn sample) were used for in situ LA-MC-ICP-MS cassiterite U-Pb dating, seven granite samples were used for bulk major and trace element analysis, and fourteen granite samples were used for bulk Sr-Nd isotope analysis. Detailed sample descriptions and analytical methods are provided in Appendix A (Table S1) and B, respectively.

4. Results

4.1. Monazite U-Th-Pb dating

The monazite grains in studied granites are subhedral to euhedral and have a size of 40–120 µm with an aspect ratio of 1:1–1:2. The well-developed growth zones within these monazites are indicative of their magmatic origin (Fig. 6a, b).

The U-Th-Pb isotopic dating results for monazites are shown in Appendix A (Table S2). The $^{208}\text{Pb}/^{232}\text{Th}$ ages of sample D1719-B1 (weakly-oriented two-mica granite) vary from 20.0 to 20.6 Ma with a weighted average age of 20.3 ± 0.1 Ma ($n = 20$, MSWD = 0.95). The $^{208}\text{Pb}/^{232}\text{Th}$ ages of sample PM02-28B4 (two-mica granite) range from 17.9 Ma to 18.5 Ma with a weighted average age of 18.3 ± 0.1 Ma ($n = 18$, MSWD = 1.14). Monazite is a Th-rich mineral and the $^{208}\text{Pb}/^{232}\text{Th}$ age data are

relatively concentrated allowing the use of the U-Th-Pb concordance diagram. In the U-Th-Pb concordance diagrams (Fig. 6a, b) almost all data points fall on or near the corresponding concordance lines, indicating that the data represent the crystallization ages of the host granites.

4.2. Muscovite Ar-Ar dating

The muscovite $^{40}\text{Ar}-^{39}\text{Ar}$ dating result for the beryl-rich pegmatite is shown in Appendix A (Table S3). Sample D8036-B9 experienced thirteen stages of heating from 700 to 1400°C. During these stages, the cumulative release of ^{39}Ar was 100%. An ideal plateau age of 15.14 ± 0.21 Ma (MSWD = 3.72) was obtained with an isochron age of 15.02 ± 0.43 Ma (MSWD = 4.45) between 800 and 1160°C (Fig. 6c, d). The initial $^{40}\text{Ar}/^{36}\text{Ar}$ ratio is 298.5 ± 11.1 . The plateau and isochron age of the muscovite sample are within error and the initial $^{40}\text{Ar}/^{36}\text{Ar}$ ratio is very close to the modern atmospheric Ar ratio (298.56 ± 0.31 ; Lee et al., 2006)). This indicates that there was no excess Ar in the tested sample and there was no significant Ar loss, i.e., muscovite has remained a closed system for K and Ar since crystallization, and was not affected by later thermal events. The analyzed age, therefore, represents a reliable crystallization age for the host pegmatite.

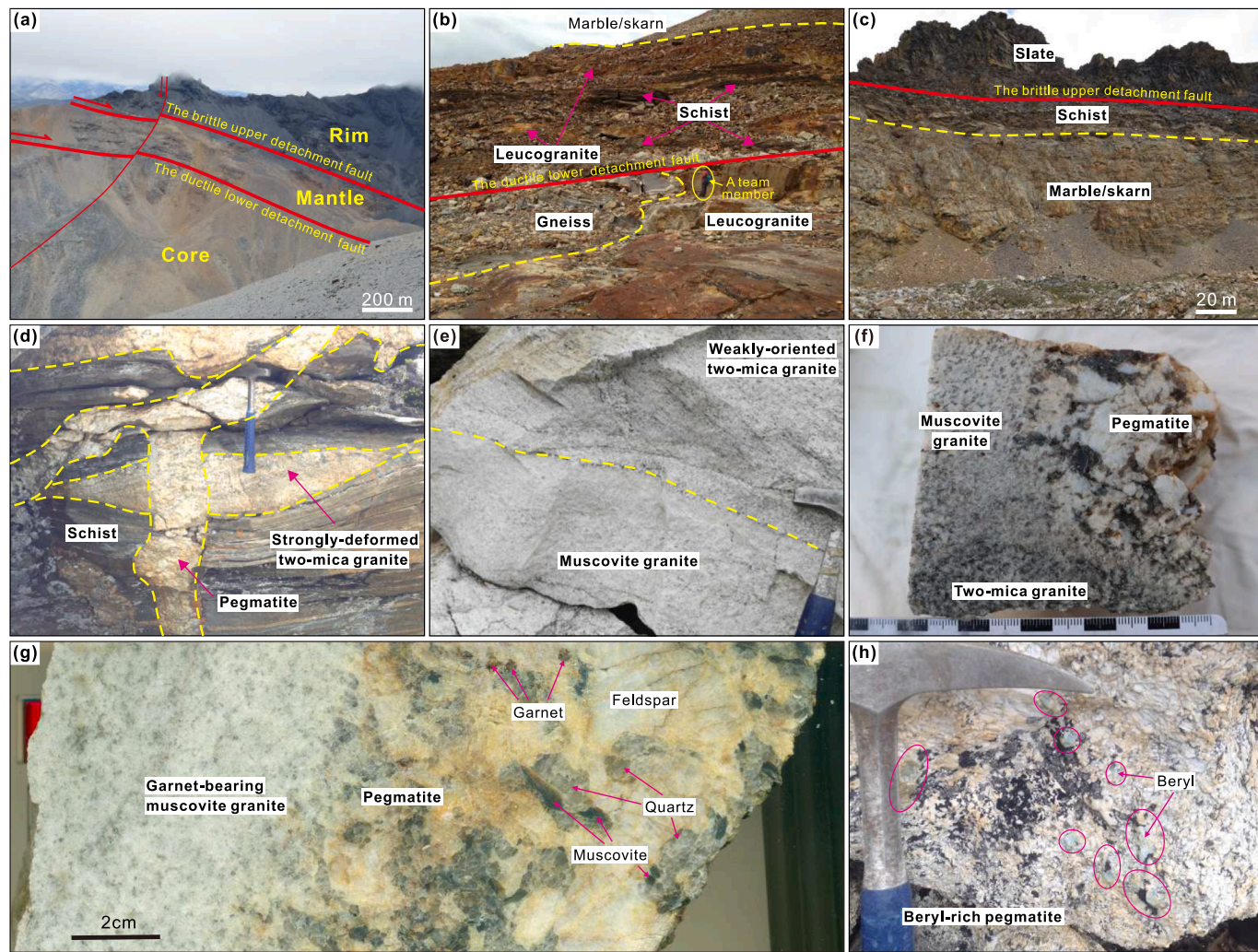


Fig. 3. (a) A macrophotograph showing that the Cuonadong dome consists of core, mantle and rim from bottom to the top separated by two detachment faults. (b) A macrophotograph showing lithologic composition of lower part of the mantle and upper part of the core. (c) A macrophotograph showing lithologic composition of upper part of the mantle and lower part of the rim. (d) An outcrop photograph showing the strongly-deformed two-mica granite was crosscut by the undeformed pegmatite. (e) An outcrop photograph showing the distinct boundary between the weakly-oriented two-mica granite and the muscovite granite. (f) A photograph of a polished rock sample showing clear boundaries between two-mica granite and muscovite granite, and between muscovite and pegmatite. (g) A photograph of a polished rock sample showing transitional boundary between muscovite granite and pegmatite. (h) An outcrop photograph of beryl-rich pegmatite.

4.3. Cassiterite U-Pb dating

The results of the cassiterite LA-MC-ICP-MS U-Pb dating for the Cuonadong Sn-W-Be polymetallic deposit are shown in Appendix A (Table S4). Sample 2019-16B1 (cassiterite-bearing greisen) has average Pb and U contents of 0.03 ppm and 17.7 ppm, respectively. The lower intercept age on the Tera-Wasserburg $^{238}\text{U}/^{206}\text{Pb}$ - $^{207}\text{Pb}/^{206}\text{Pb}$ (T-W) diagram is 17.1 ± 0.3 Ma (MSWD = 2.6, n = 34) (Fig. 7a). Sample 2019-31B1 (cassiterite-bearing greisen) has average Pb and U contents of 0.17 ppm and 25 ppm, respectively. The lower intercept age on the T-W diagram is 17.9 ± 0.3 Ma (MSWD = 2.6, n = 42) (Fig. 7b). Sample DZW02 (cassiterite-bearing greisen) has average Pb and U contents of 0.19 ppm and 1.46 ppm, respectively. The lower intercept age on the T-W diagram is 18.3 ± 0.8 Ma (MSWD = 2.4, n = 36) (Fig. 7c). Sample D8036-B3-2 (cassiterite-bearing skarn) has an average Pb and U contents of 0.02 and 7.54 ppm, respectively. The lower intercept age on the T-W diagram is 13.9 ± 0.6 Ma (MSWD = 3.1, n = 30) (Fig. 7c), which is similar to the age of another cassiterite grain (D8036-B3, 14.2 ± 0.2 Ma) within the same thin section as reported by Cao et al. (2021b).

4.4. Whole-rock major and trace elements

The major and trace element compositions for the Cuonadong leucogranites are presented in Appendix A (Table S5), including seven samples from this study and 18 samples from Huang (2019). The Cuonadong leucogranites display similar major element compositions and show high contents of SiO_2 (71.62–75.97 wt%), Al_2O_3 (14.04–16.09 wt %), total alkali ($\text{K}_2\text{O} + \text{Na}_2\text{O}$) = 7.71–8.84 wt%), and low concentrations of MgO (0.07–0.33 wt%), TiO_2 (0.01–0.12 wt%) and total iron ($\text{Fe}_{2\text{O}}^{\text{T}}$ = 0.36–1.01 wt%). The differentiation index ($\text{DI} = \text{Quartz} + \text{Orthoclase} + \text{Albite} + \text{Nepheline} + \text{Leucite} + \text{K-feldspar}$, from CIPW calculating values) is 90.67–94.75. The A/CNK ratio (molar ratio of $\text{Al}_2\text{O}_3/[\text{CaO} + \text{K}_2\text{O} + \text{Na}_2\text{O}]$) varies between 1.09 and 1.22 whereas the A/NK ratio (molar ratio of $\text{Al}_2\text{O}_3/[\text{K}_2\text{O} + \text{Na}_2\text{O}]$) ranges between 1.17 and 1.42 (average of 1.32), showing strong peraluminous characteristics (Fig. 8a). The $([\text{K}_2\text{O} + \text{Na}_2\text{O}]/\text{CaO})$ values vary from 6.65 to 8.28 wt% indicating medium-K calc-alkalic to high-K alkali-calcic series (Fig. 8b). In the AFC diagram, all samples are located in peraluminous or S-type granite field (Fig. 8c).

The total rare earth element (ΣREE) contents of the Cuonadong leucogranites are relatively low and vary between 20.27 and 112.9 ppm.

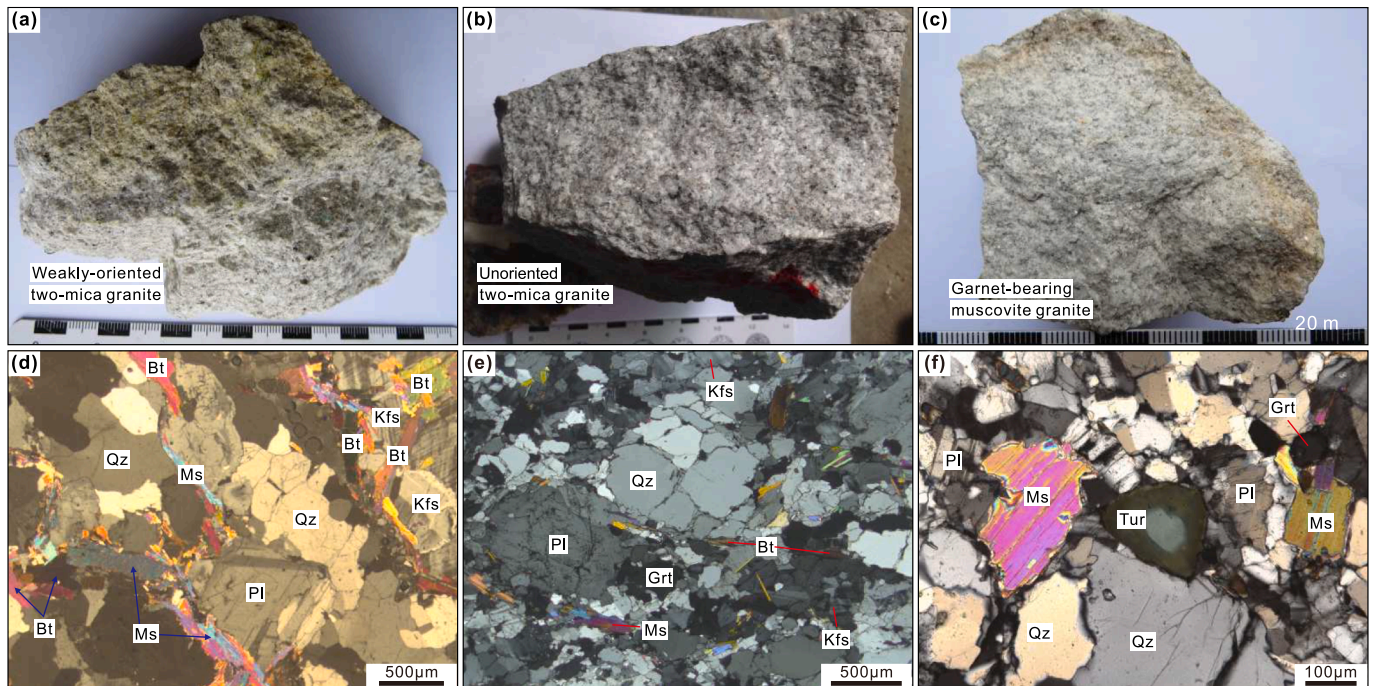


Fig. 4. Photographs and microphotographs of representative samples of (a, d) weakly-oriented two-mica granite, (b, e) two-mica granite, and (c, f) muscovite granite. Microphotographs were captured under crossed polarized light. Qz: quartz; Bt: biotite; Ms: muscovite; Kfs: potassium feldspar; Pl: plagioclase; Grt: garnet; Tur: tourmaline.

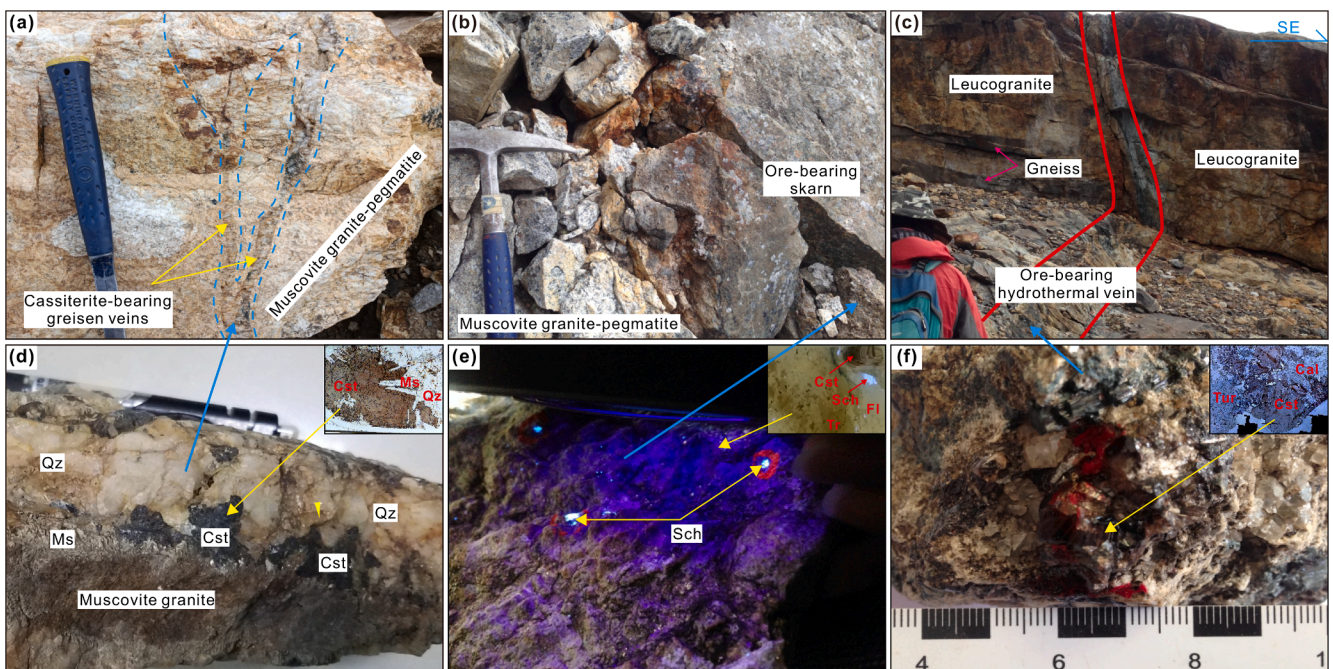


Fig. 5. (a) An outcrop photograph of cassiterite-bearing greisen vein that developed in muscovite granite-pegmatite. (b) An outcrop photograph of ore-forming skarn that developed at the contact zone between muscovite granite/pegmatite and marble. (c) A macrophotograph showing an ore-bearing hydrothermal vein that crosscuts leucogranite. (d-f) Photographs of representative greisen-type, skarn-type, and hydrothermal vein-type rare-metal ores from the Cuonadong Sn-W-Be polymetallic deposit. Qz: quartz; Ms: muscovite; Tur: tourmaline; Cst: cassiterite; Sch: scheelite; Fl: fluorite; Tr: tremolite; Cal: calcite.

The average ΣREE contents of the weakly-oriented two-mica granite, two-mica granite, and the muscovite granite are 73.85, 31.02, and 30.85 ppm, respectively. These leucogranites are enriched in light rare earth elements (LREE) but depleted in heavy rare earth elements (HREE) ($\text{LREE/HREE} = 1.14\text{--}13.93$), and display significant and variable negative Eu anomalies ($\text{Eu/Eu}^* = 0.04\text{--}0.80$) (Table S5; Fig. 9a, c, e).

Importantly, the REE pattern becomes flatter and the negative Eu anomalies increases from the weakly-oriented two-mica granite through the two-mica granite to the muscovite granite (Fig. 9a, c, e). On the chondrite-normalized REEs patterns, the two-mica granite and muscovite granite samples show an evident W-type REE tetrad effect (Fig. 9a, c, e; Irber, 1999). The intensity of the REE tetrad effect is quantified by

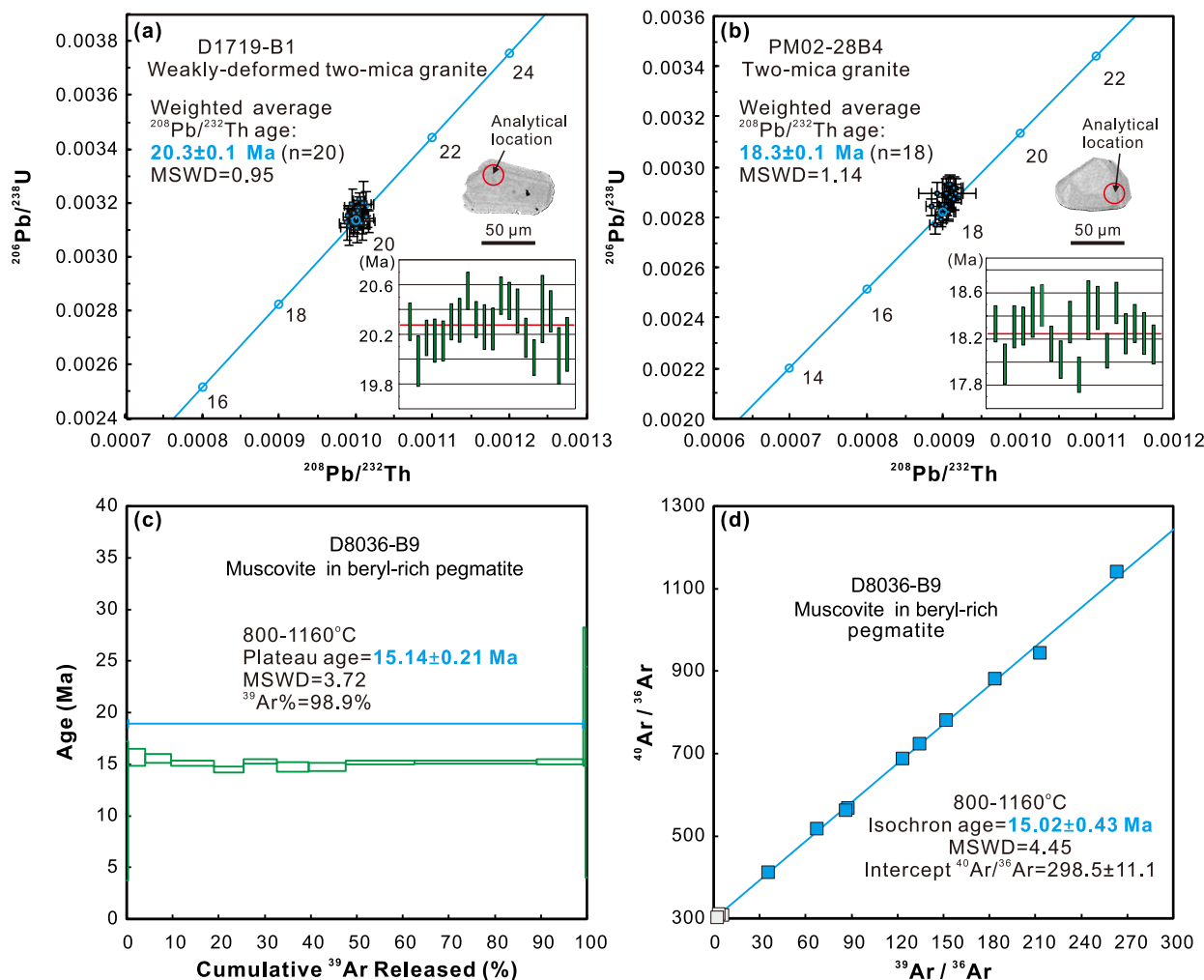


Fig. 6. Monazite U-Th-Pb concordia diagrams and backscattered electron images of representative monazite grains in (a) weakly-oriented two-mica granite and (b) two-mica granite; (c) Muscovite ^{40}Ar - ^{39}Ar plateau age and (d) isochron age plots for the beryl-rich pegmatite from the Cuonadong Sn-W-Be polymetallic deposit.

the TE_{1,3} value ($\text{TE}_{1,3} = [(\text{Ce} \times \text{Pr} \times \text{Tb} \times \text{Dy})_{\text{N}} / (\text{La} \times \text{Nd} \times \text{Gd} \times \text{Ho})_{\text{N}}]^{1/4}$), where TE_{1,3} values > 1.1 indicate a tetrad effect (Irber, 1999). The TE_{1,3} values of the weakly-oriented two-mica granite, two-mica granite, and the muscovite granite are 0.99–1.12 (1.08 on average), 1.13–1.17 (1.15 on average), and 1.16–1.25 (1.20 on average) (Table S5), respectively. Thus, the REE tetrad effect increases from the weakly-oriented two-mica granite to the two-mica granite, and the muscovite granite.

The Cuonadong leucogranites are relatively enriched in large ion lithophile elements (e.g., Rb, U, and Pb) and depleted in high field strength elements (e.g., Nb, Zr, and Ti) (Fig. 9b, d, f). They show significant negative Ba and Sr anomalies, which increase from the weakly-oriented two-mica granite to the two-mica granite and muscovite granite. In addition, the muscovite granite also displays perceptible negative P anomalies (Fig. 9f).

4.5. Whole-rock Sr-Nd isotopes

Sr-Nd isotopic data of the Cuonadong leucogranites are shown in Appendix A (Table S6), including 14 samples from this study and 11 samples from Huang (2019). The initial $^{87}\text{Sr}/^{86}\text{Sr}$ ratios [$(^{87}\text{Sr}/^{86}\text{Sr})_i$] were calculated for an age of 15 Ma (the youngest age for the Cuonadong leucogranites; Cao et al., 2021b). The results show that the $(^{87}\text{Sr}/^{86}\text{Sr})_i$ values of the weakly-oriented two-mica granite range between 0.719566 and 0.734390, with corresponding $\epsilon_{\text{Nd}}(t)$ values ranging between -13.7 and -11.7 and two-stage Nd model ages (T_{DM2}) of 1.78–1.94 Ga. The $(^{87}\text{Sr}/^{86}\text{Sr})_i$ of the two-mica granite varies from 0.723421 to 0.757158,

with corresponding $\epsilon_{\text{Nd}}(t)$ values of -15.7 to -12.0 and two-stage Nd model ages of 1.81–2.10 Ga. The $(^{87}\text{Sr}/^{86}\text{Sr})_i$ ratios of the muscovite granite range from 0.747657 to 0.763132, with corresponding $\epsilon_{\text{Nd}}(t)$ values of -15.7 to -13.1 and two-stage Nd model ages of 1.89–2.10 Ga.

5. Discussion

5.1. Timing framework of magmatism and rare-metal mineralization in Cuonadong

Available published geochronological data show that except for minor strongly-deformed leucogranites/pegmatites that were formed at ~ 35 –24 Ma (Fu et al., 2020; Zhang et al., 2020; He et al., 2022), the major leucogranites/pegmatites in the Cuonadong dome were formed during ~ 21 –15 Ma (Cao et al., 2021b; Chen et al., 2021; He et al., 2022, and references therein). Monazites collected from the weakly-oriented two-mica granite and the undeformed two-mica granite in Cuonadong yielded crystallization ages of ~ 20 Ma and ~ 18 Ma, respectively (Fig. 6a and b). The muscovite ^{40}Ar - ^{39}Ar dating result indicates that the beryl-rich pegmatite was formed/cooled at ~ 15 Ma (Fig. 6c and d). Noteworthily, the pegmatite represents a magmatic-hydrothermal transitional phase due to coexisting of melt and fluid inclusions (Xie et al., 2017). Thus, geochronological data in this study indicate that the major Cuonadong leucogranites were generated at ~ 20 –15 Ma, which is highly consistent with previous results. Thus, a long-term magmatism (~ 6 Ma) generated the major Cuonadong leucogranites.

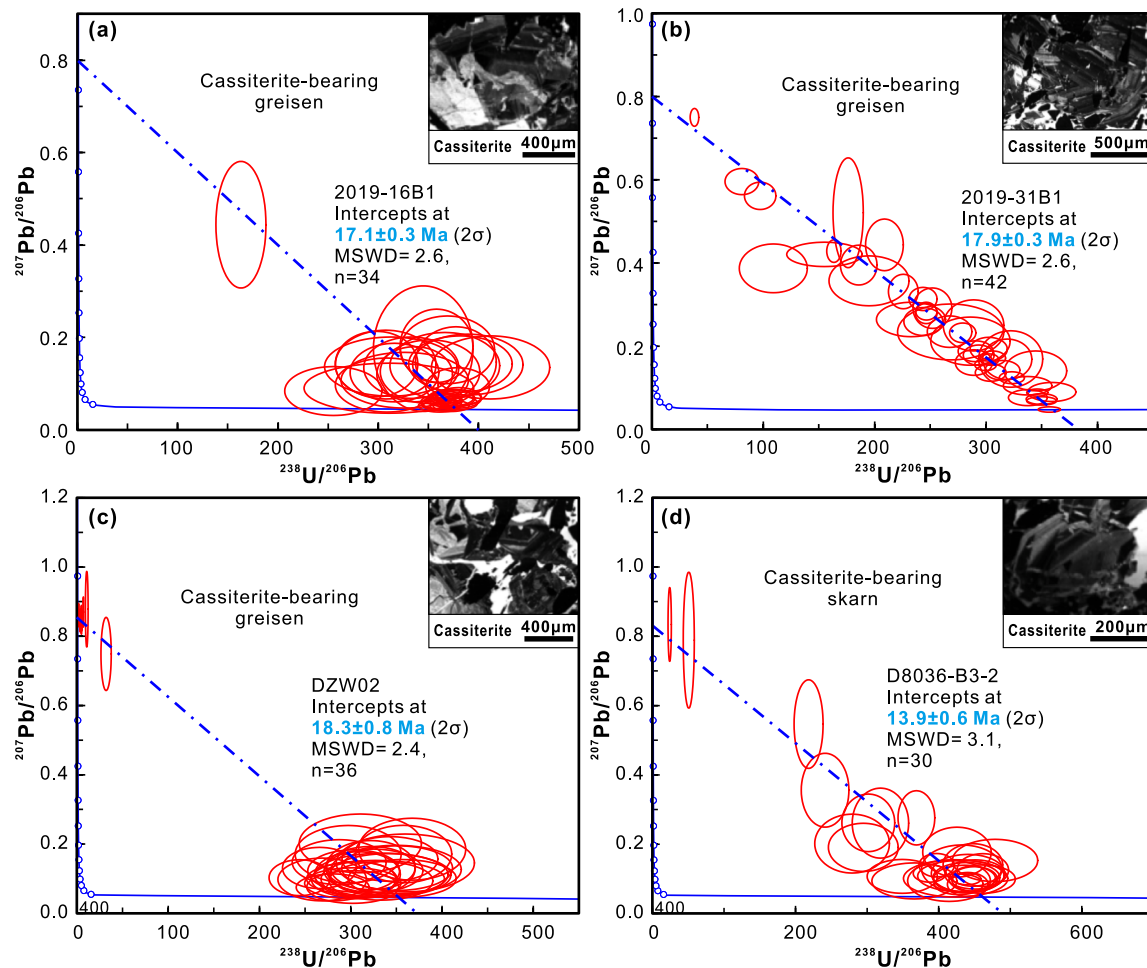


Fig. 7. Tera-Wasserburg (T-W) concordia plots of in-situ U-Pb dating results and cathodoluminescence images of cassiterite in (a-c) greisen, and (d) skarn from the Cuonadong Sn-W-Be polymetallic deposit.

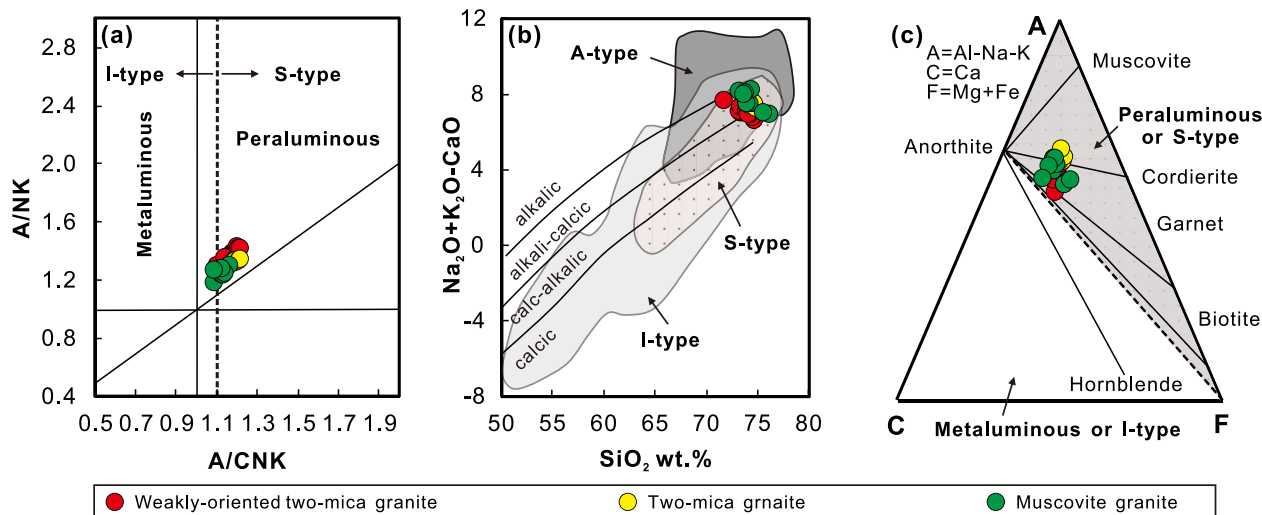


Fig. 8. (a) A/NK versus A/CNK (after Maniar and Piccoli, 1989), (b) (Na₂O + Na₂O□CaO) versus SiO₂ (after Frost et al., 2001) and (c) AFC diagrams (after Chappell and White, 1992) for the Cuonadong leucogranites.

Although the isotopic ages of the major Cuonadong leucogranites are partly overlapping (Cao et al., 2021b; Chen et al., 2021; He et al., 2022, and references therein), the old-young relationships of these leucogranites can be readily determined based on combined consideration of

geochronological data and field observations. Undoubtedly, the weakly-oriented two-mica granite should have formed earlier than undeformed/unoriented two-mica and muscovite granites. In addition, the muscovite granite should have generated later than other granites considering the

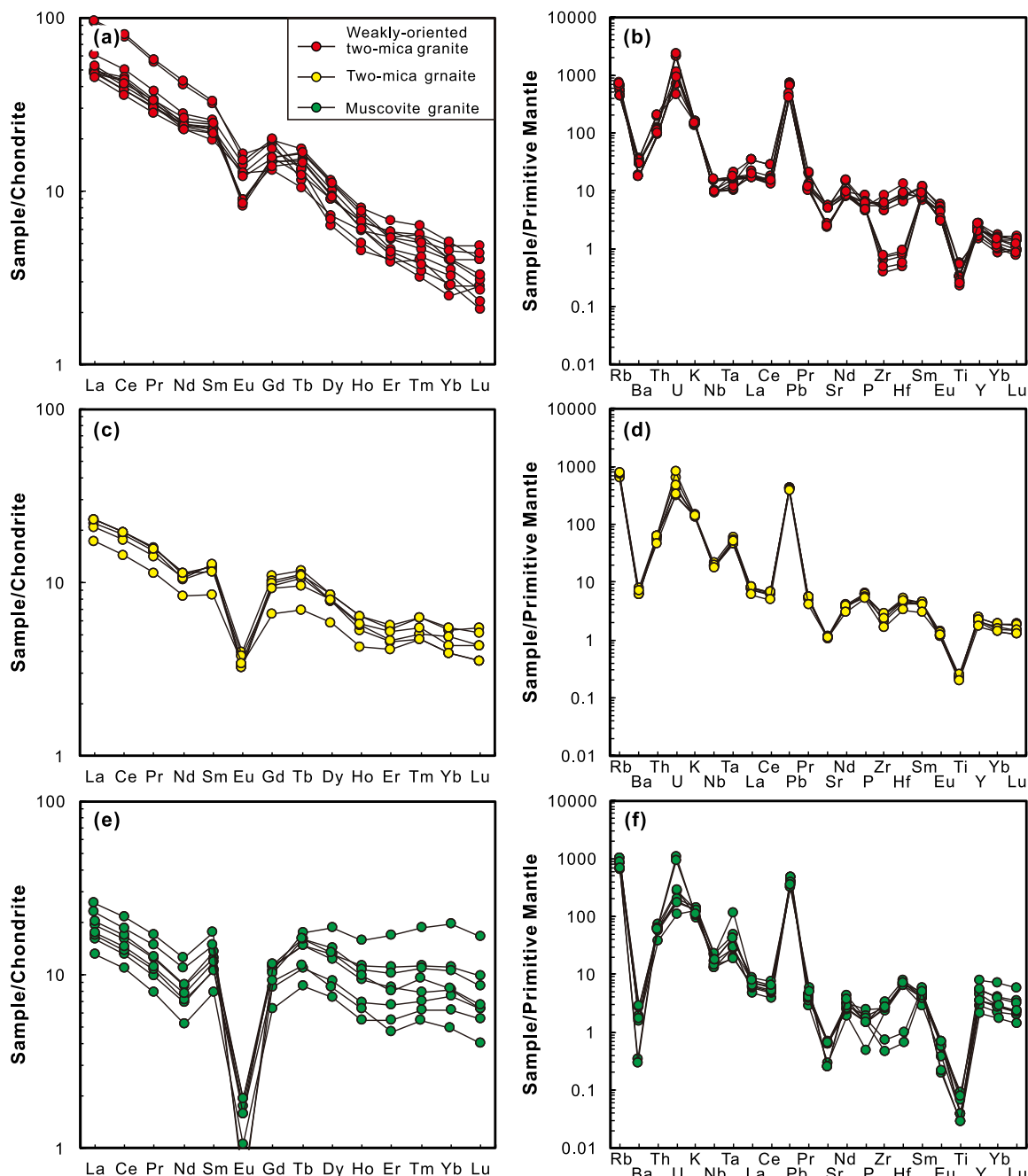


Fig. 9. (a, c, e) Chondrite-normalized REEs patterns and (b, d, f) primitive mantle-normalized trace elements patterns for the Cuonadong leucogranites. Chondrite values are from Sun and McDonough (1989).

youngest isotopic ages (~ 15 Ma) for the Cuonadong leucogranites in the literature are always from the muscovite granite (Cao et al., 2020, 2021b). Moreover, the transitional boundary between the muscovite granite and pegmatite (Fig. 3g) indicates that the muscovite granite was the latest magmatic product in the Cuonadong dome. Consequently, the weakly-oriented two-mica granite, the undeformed two-mica granite and the muscovite granite should have formed successively.

Greisen-hosted cassiterites from the Cuonadong deposit yield ages of 17.1 ± 0.3 Ma (sample 2019-16B1; Fig. 7a), 17.9 ± 3 Ma (sample 2019-31B1; Fig. 7b) and 18.3 ± 0.8 Ma (sample DZW02; Fig. 7c), indicating that remarkable greisen-type Sn mineralization occurred at 17–18 Ma. The skarn-hosted cassiterite yield an age of 13.9 ± 0.6 Ma (sample D8036-B3-2; Fig. 7d) representing the timing for skarn-type rare-metal mineralization. The muscovite Ar-Ar age (~ 15 Ma; Fig. 6c, d) of the

beryl-rich pegmatite (sample D8036-B9) represents the timing for the pegmatitic Be mineralization. Together with published ore-forming geochronological data (Cao et al., 2020, 2021b; Xie et al., 2020; Dai et al., 2022; He et al., 2022), we propose that the Cuonadong Sn-W-Be polymetallic deposit has experienced a long-lasting mineralization process of ~ 4 Ma (18–14 Ma).

Timing framework of magmatism and mineralization within an ore district commonly plays a significant role in determining their genetic correlations (Xu et al., 2017; Cao et al., 2019; Fei et al., 2020). Generally, the lifespan of a magmatic-hydrothermal system is < 10 million years, and even shorter (< 2 Ma) for porphyry deposits (Petford et al., 2000; Glazner et al., 2004; Chiaradia et al., 2013; Karakas et al., 2017; Li et al., 2017b). Accordingly, a time interval of > 10 Ma between plutons and mineralization is interpreted to indicate that they have no genetic

ties (Fei et al., 2020). Therefore, the 35–24 Ma-aged leucogranites are unlikely the causative intrusion for the Cuonadong Sn-W-Be polymetallic deposit. In contrast, leucogranite(s) that formed during 21–15 Ma was likely the ore-forming granite. Obviously, the muscovite granite should be the direct ore-related granite considering its intimate relationship with the orebodies (Fig. 5a-c).

5.2. Magma source of the Cuonadong leucogranites

The geochemical compositions of granites can provide insights into the origin of the magma source. The Cuonadong leucogranites display similar geochronological features, indicating similar magma source. In general, these leucogranites have high SiO₂ (71.62–75.97 wt%) and Al₂O₃ (14.04–16.09 wt%) and low MgO (0.07–0.33 wt%), MnO (0.01–0.15 wt%) and total iron (Fe₂O₃^T = 0.36–1.01 wt%) contents (Table S5). They are enriched in large ion lithophile elements (e.g., Rb, U, K, and Pb), and relatively depleted in high field strength elements (e.g., Nb, Zr, and Ti) (Fig. 9; Table S5), which are the geochemical characteristics of crust-derived rocks (Rudnick and Gao, 2003). More specific information regarding magma source can be revealed by some major and trace element discriminant diagrams. On the Rb/Sr vs. Rb/Ba plot, the Cuonadong leucogranites fall entirely in the clay-rich source region (Fig. 10a; Sylvester, 1998). Similarly, on the Al₂O₃ + Fe₂O₃^T + MgO + TiO₂ vs. Al₂O₃/(Fe₂O₃^T + MgO + TiO₂) diagram, these granites also plot mainly in/near the felsic pelite field (Fig. 10b; Patiño Douce, 1999). Thus, the Cuonadong leucogranites were likely derived from partial melting of clay-rich sedimentary rocks.

Besides geochemical compositions, the Sr-Nd isotopes play a significant role in determining magma source. For instance, similar Sr-Nd isotopic compositions of the Eocene high Sr/Y granites in the Yardoi area and the amphibolites (typical rocks of lower crust in this region) nearby suggest their genetic relationships (Zeng et al., 2011; Hou et al., 2012; Dai et al., 2020). The Sr-Nd isotopes of the Cuonadong leucogranites differ from those of the amphibolite-derived Eocene high Sr/Y granites in the Yardoi area (Fig. 11), excluding the possibility of amphibolites as the major source rocks for the Cuonadong leucogranites. In contrast, the Cuonadong leucogranites show Sr-Nd isotopic compositions similar to those of the metapelites of the Higher Himalayan Crystalline Sequence and the Tethyan Himalaya Sequence (Fig. 11; Dai et al., 2020 and references therein). Considering the higher position of the Tethyan Himalaya Sequence compared to the Cuonadong leucogranites (Fig. 2), the Tethyan Himalaya metapelites could not have been the

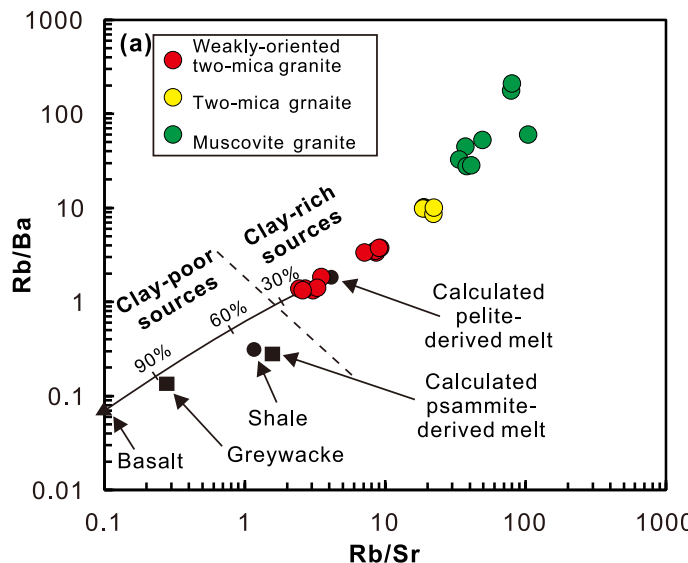


Fig. 10. (a) Rb/Ba versus Rb/Sr (after Sylvester, 1998) and (b) Al₂O₃ + Fe₂O₃^T + MgO + TiO₂ vs. Al₂O₃/(Fe₂O₃^T + MgO + TiO₂) diagrams (after Patiño Douce, 1999) for the Cuonadong leucogranites.

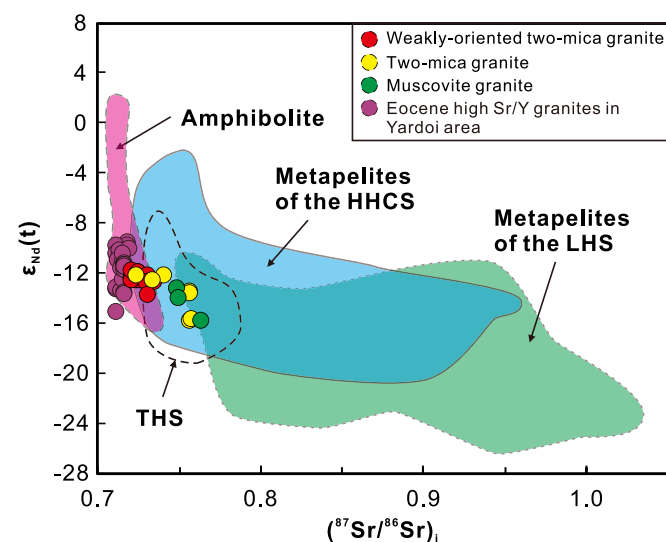


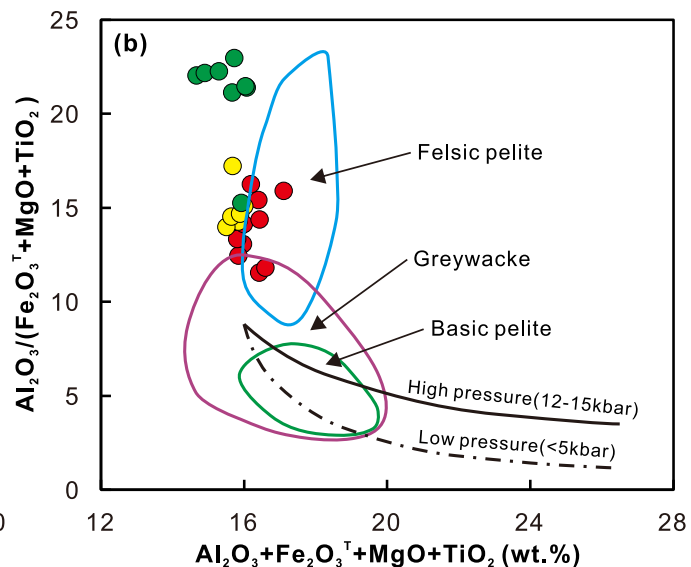
Fig. 11. ε_{Nd}(t) versus ⁸⁷Sr/⁸⁶Sr diagram for the Cuonadong leucogranites. Data sources: Metapelites of HHCS, metapelites of LHS, low-grade metamorphic or unmetamorphosed sedimentary rocks of THS and Late Eocene adakitic granites with high Sr/Y granites are from Dai et al. (2020) and references therein; amphibolites (including garnet-amphibolite from the Yardoi area and amphibolite from Cuonadong) are from Zeng et al. (2011) and Zhang et al. (2021). (⁸⁷Sr/⁸⁶Sr)_i and ε_{Nd}(t) values were normalized to 15 Ma.

source for the Cuonadong leucogranites. Consequently, the metapelites of the Higher Himalayan Crystalline Sequence were most likely the main magma source.

It can, therefore, be concluded that the source region of the Cuonadong leucogranites was composed of metapelites of the High Himalayan Crystalline Sequence based on their compositional and isotopic features.

5.3. Petrogenesis of the Cuonadong leucogranites

The I-S-(M)-A classification is one of the most prevailing classification schemes for granitoids (Whalen et al., 1987; Chappell and White, 1992). Genetically, rare-metal deposits can be related to all these granite types (Li et al., 2018; Zhao et al., 2018; Yan et al., 2020; Romer and Pichavant, 2021). Obviously, the peraluminous features and origin of



metapelites suggest that the Cuonadong leucogranites are S-type granites (Chappell and White, 1992). This conclusion is also supported by lines of other evidence as follows. A-type granites are typically characterized by presence of anhydrous minerals (pyroxene and fayalite) and are enriched in HFSEs with high crystallization temperature (approximately to 830 °C; Whalen et al., 1987; Bonin, 2007). However, pyroxene and fayalite do not occur in Cuonadong leucogranites (Fig. 4d-f). HFSE depletion (Fig. 9) and the relatively low crystallization temperature ($T_{\text{cr}} = 637\text{--}754^{\circ}\text{C}$; Lin et al., 2016b; Huang et al., 2018) preclude an A-type affinity. On the $(\text{Na}_2\text{O} + \text{K}_2\text{O})/\text{CaO}$ vs. $\text{Zr} + \text{Nb} + \text{Ce} + \text{Y}$ and $10000^*\text{Ga}/\text{Al}$ vs. $\text{Zr} + \text{Nb} + \text{Ce} + \text{Y}$ discrimination diagrams, samples mainly plot near or within the field of fractionated M-, I- and S-type granite (Fig. 12a, b). The presence of muscovite, garnet, and tourmaline in the Cuonadong leucogranites (Fig. 4d-f) implies their S-type attributes

(Chappell and Simpson, 1984; Chappell and White, 1992). This is reinforced by S-type trends of these leucogranites on the Th vs. Rb and La vs. Rb plots (Fig. 12c, d).

Generally, the metasedimentary rocks-derived Himalayan leucogranites can be generated through three different crustal anatexis styles: fluid-fluxed melting of muscovite, fluid-absent melting of muscovite or biotite (Gou et al., 2016, 2019; Gao et al., 2017). Biotite is a Ti-, Fe-, and Mg-rich mineral, so the dehydration-melting of biotite generates melts with relatively high contents of TiO_2 , total Fe_2O_3 and MgO (Gou et al., 2016, 2019). Besides, breakdown of biotite occurs at a relatively higher temperature threshold than muscovite, e.g., at 1 GPa breakdown of biotite and muscovite decompose at 800 °C and 750 °C, respectively (Gardien et al., 1995). The low TiO_2 (0.01–0.12 wt%), total Fe_2O_3 (0.36–1.01 wt%) and MgO (0.07–0.33 wt%) contents and low zircon

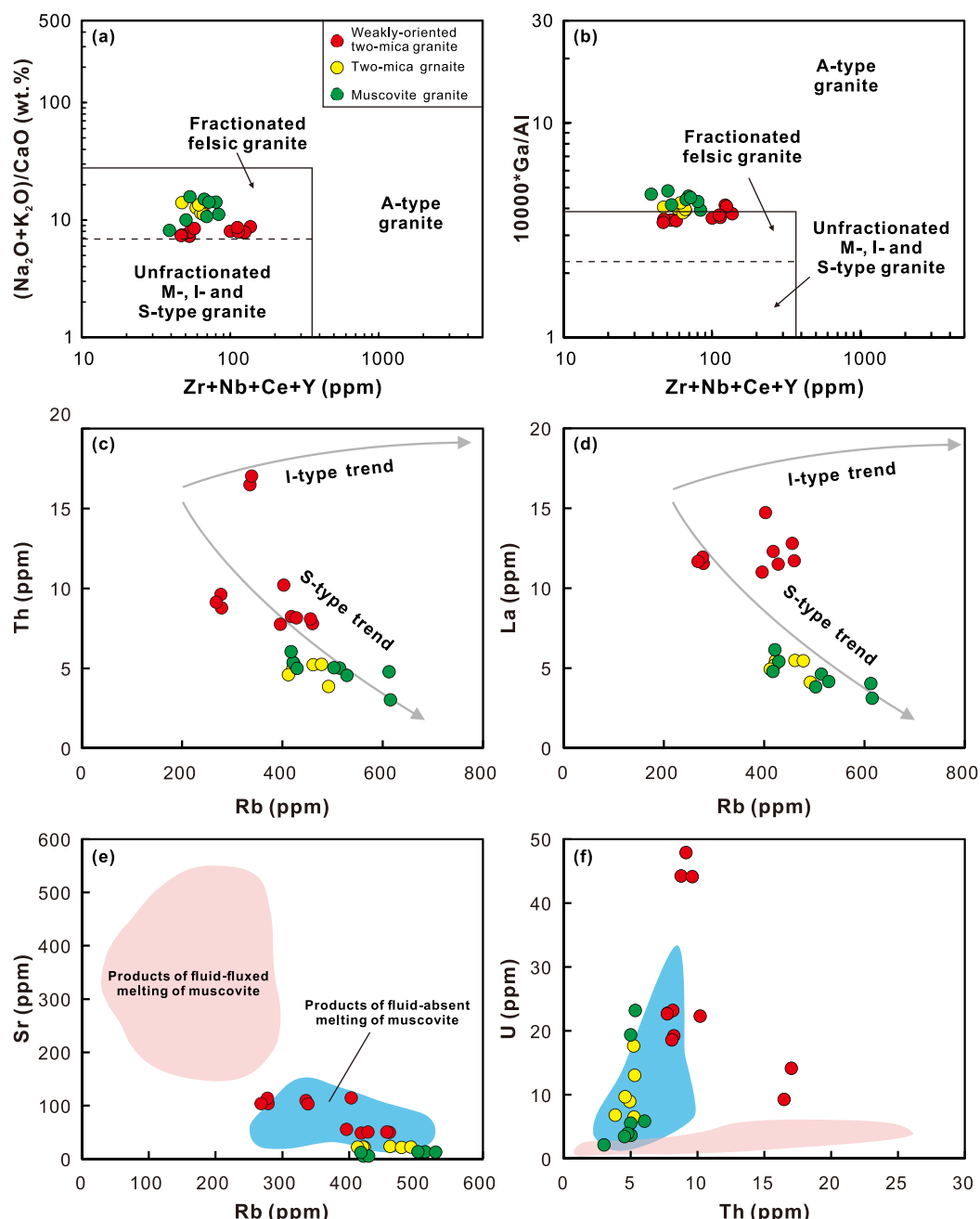


Fig. 12. (a) $(\text{Na}_2\text{O} + \text{K}_2\text{O})/\text{CaO}$ vs. $\text{Zr} + \text{Nb} + \text{Ce} + \text{Y}$ (after Whalen et al., 1987), (b) $10000^*\text{Ga}/\text{Al}$ vs. $\text{Zr} + \text{Nb} + \text{Ce} + \text{Y}$ (after Eby, 1990), (c) Th versus Rb (after Chappell, 1999), (d) La versus Rb (after Zhang et al., 2019b), (e) Sr vs. Rb (after Gao et al., 2017) and (f) U vs. Th (after Gao et al., 2017) plots for the Cuonadong leucogranites.

saturation temperature ($T_{\text{zr}} = 637\text{--}754^{\circ}\text{C}$; Lin et al., 2016a; Huang et al., 2018) preclude the possibility of biotite dehydration-melting. In contrast, high Rb (268–615 ppm), U (2–48 ppm), low Sr (5–115 ppm), Th (3–17 ppm) contents and high Rb/Sr (2–104) and U/Th (0.6–5) mass ratios imply that the Cuonadong leucogranites were most likely derived from muscovite dehydration-induced partial melting of metapelites (Fig. 12e and f; Wang et al., 2015; Gao et al., 2017).

Rb is more incompatible than Sr in magmatic systems, particularly in high-silica granites, leading to continuous increase in Rb/Sr values with crystallization differentiation of granites (Lee and Morton, 2015). Thus, Rb/Sr can be used as a differentiation proxy, since SiO_2 decreases in extremely evolved systems (Romer and Pichavant, 2021). From the old weakly-oriented two-mica granite through the two-mica granite to the young muscovite granite, the Rb/Sr ratios increase significantly (Fig. 10a), suggesting progressive degrees of magmatic fractionation. This is supported by the perceptible linear relations between some major elements and Rb/Sr values (Fig. 13). The muscovite granite was formed at the latest stage and have highest Rb/Sr values and DI (average DI = 93.67; Table S5), thus experienced the highest degree of differentiation.

In contrast, the weakly-oriented two-mica granite was formed at the earliest stage and has lowest Rb/Sr ratios and DI (average DI = 91.17; Table S5), thus experienced lowest degree of differentiation. Therefore, the weakly-oriented two-mica granite samples with lowest Rb/Sr ratios (CND0205 and CND0206; Table S5) have geochemical compositions relatively close to those of the primitive magma that formed the Cuonadong leucogranites. Assuming the average composition of these two samples to represent the primitive magma composition, we carried out quantitative fractional crystallization simulation calculations based on the whole-rock Rb, Sr, and Ba contents using Rb, Sr, Ba partition coefficients proposed by Rollinson (1993). The results show that the weakly-oriented two-mica granite, undeformed two-mica granite, and the muscovite granite can be generated by 0–40%, 40–60% and 50–80% fractional crystallization of a mineral assemblage of 25% plagioclase + 55% K-feldspar + 20% biotite, respectively (Fig. 14).

From the weakly-oriented two-mica granite to the undeformed two-mica granite and the muscovite granite, the increasing negative Ti anomalies (Fig. 9b, d, f) indicate that fractional crystallization of Ti-bearing minerals probably played a role in changing residual magma

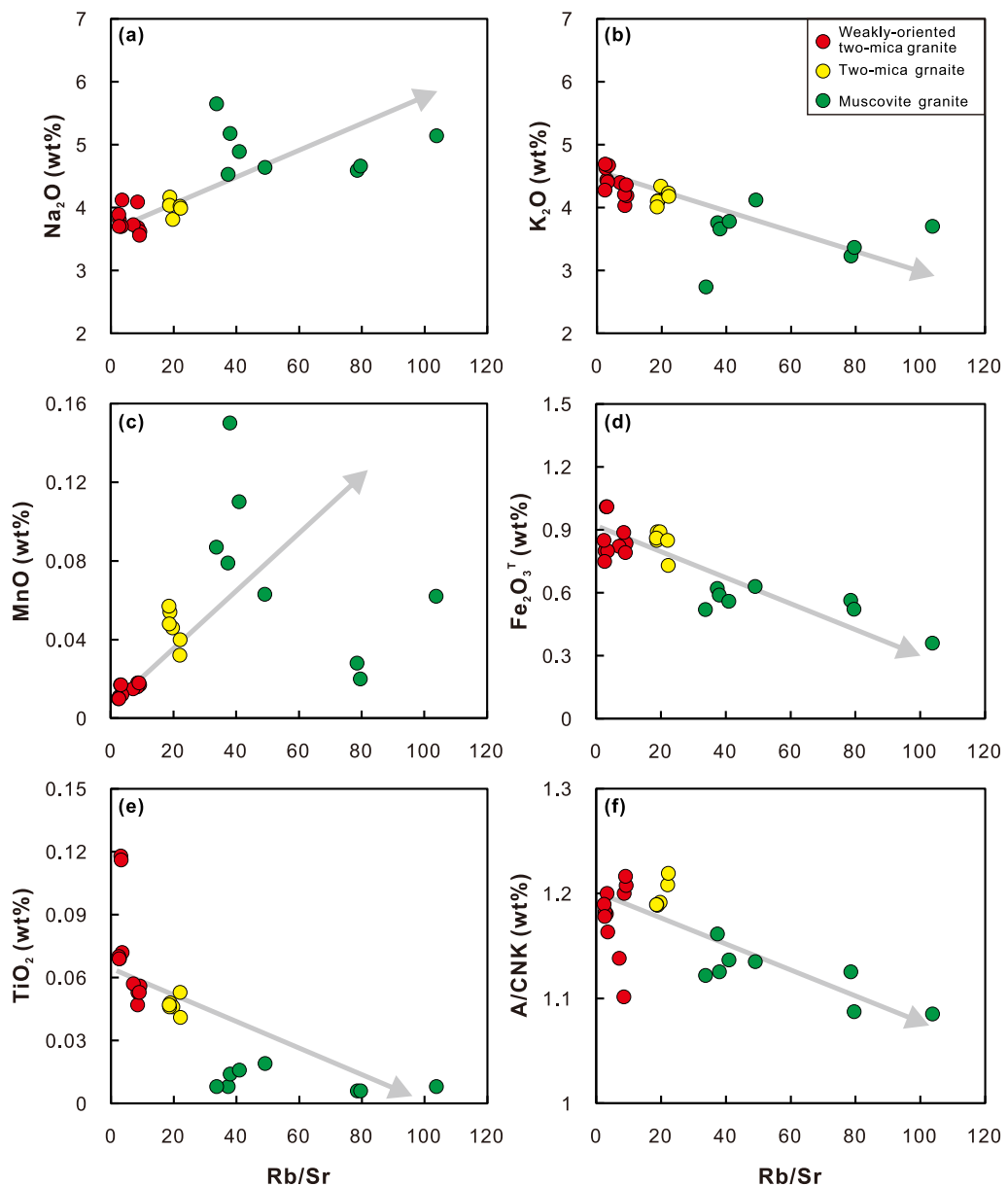


Fig. 13. (a) Na_2O , (b) K_2O , (c) MnO , (d) Fe_2O_3^T , (e) TiO_2 , (f) A/CNK vs. Rb/Sr plots for the Cuonadong leucogranites.

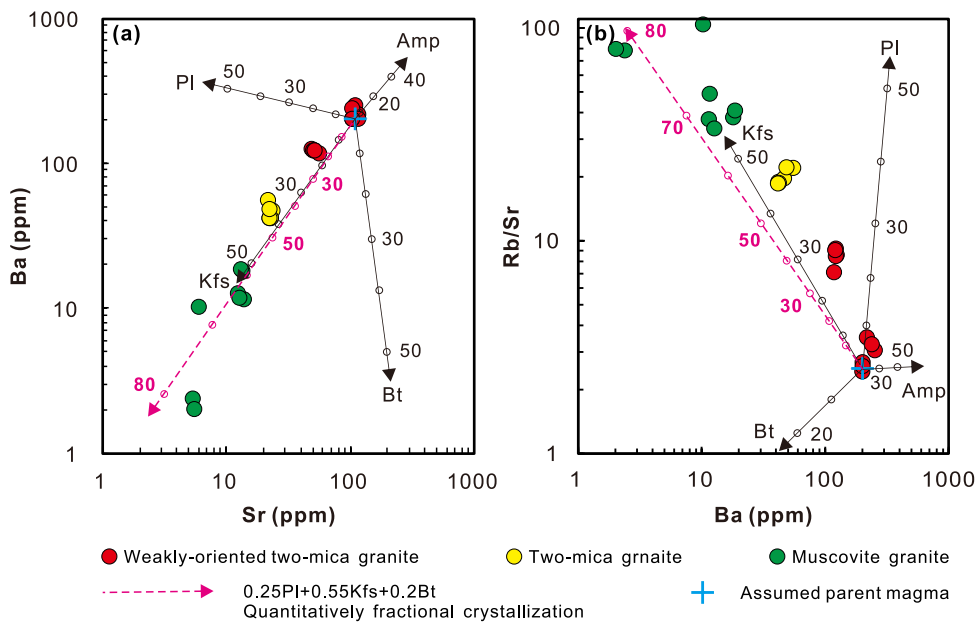


Fig. 14. (a) Log-log diagrams of Ba versus Sr and (b) Rb/Sr versus Ba, showing fractionation of minerals, which controlled the variation of these elements from weakly-oriented two-mica granite via two-mica granite to muscovite granite in Cuonadong. The least fractionated magma is represented by the average composition of two least fractionated samples of the weakly-oriented two-mica granite with the lowest Rb/Sr ratio (CND0205 and CND0206) from Huang (2019). Partition coefficients are from Rollinson (1993). Amp: amphibole; Bt: biotite; Kfs: potassium feldspar; Pl: plagioclase.

composition. Similarly, visible negative P anomalies of the muscovite granite (Fig. 9f) implies that the fractional crystallization of P-bearing minerals (such as monazite and apatite) probably occurred during magma evolution (Chen et al., 2015; Dai et al., 2020). The decreasing LREE contents from the weakly-oriented two-mica granite to the two-

mica granite and the muscovite granite (Fig. 8a, c, e) are in accordance with fractional crystallization of LREE-rich minerals such as monazite (Stepanov et al., 2012).

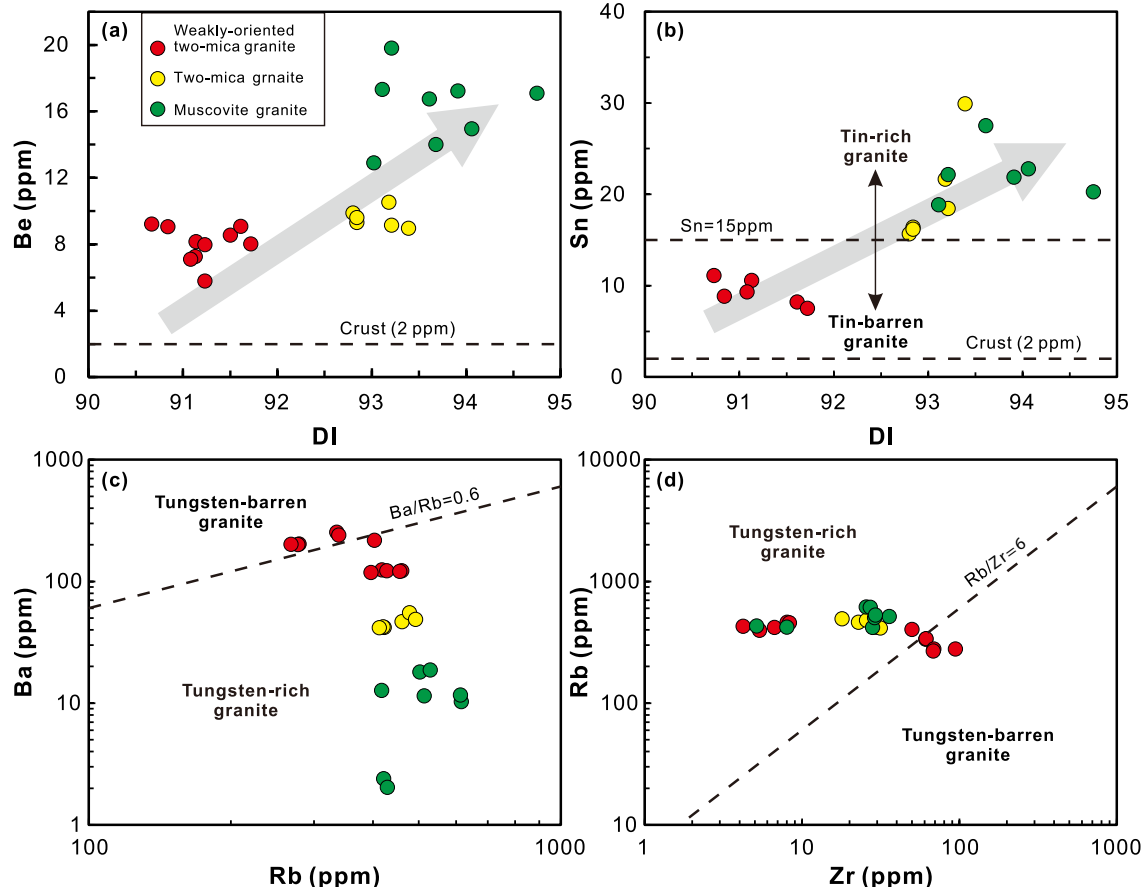


Fig. 15. (a) Be and (b) Sn vs. differentiation index (DI) plots and (c) Ba and (d) Zr vs. Rb plots for the Cuonadong leucogranites. The crustal values of Be and Sn are from Rudnick and Gao (2003), while the boundaries between the Sn-rich and Sn-poor granites and between the W-rich and W-poor granites are from Lehmann (1990) and Huang and Jiang (2013), respectively.

5.4. Implications for rare-metal mineralization in Cuonadong

Generally, breakdown of rare metal-enriched minerals (e.g., micas; Kunz et al., 2022) during partial melting of metapelites in the source region can produce melts that are rich in these elements, while fractional crystallization can further enrich the residual melts with these incompatible rare metals (Evensen and London, 2003; Simons et al., 2017; Zhang et al., 2019c). As demonstrated above, the S-type Cuonadong leucogranites stemmed from metapelites of HHCS via muscovite dehydration melting. However, the Sn (7.5–11.1 ppm), W (2.2–3.3, except

one sample having W content of 14.1 ppm), and Be (5.8–9.2 ppm, except one sample having Be content of 29.1 ppm) contents of the relatively primitive magma (as represented by the weakly-oriented two-mica granite) are just a little higher than the bulk continental crust (Sn = 1.7 ppm, W = 1.0 ppm, Be = 1.9 ppm; Rudnick and Gao, 2003) (Table S5). This implies that remarkable enrichment of these rare metals did not occur during partial melting. Thus, the significant enrichment of rare-metal elements could have occurred during magma evolution (fractional crystallization). Obviously, the increasing contents of Be and Sn with increasing differentiation index is consistent with this deduction

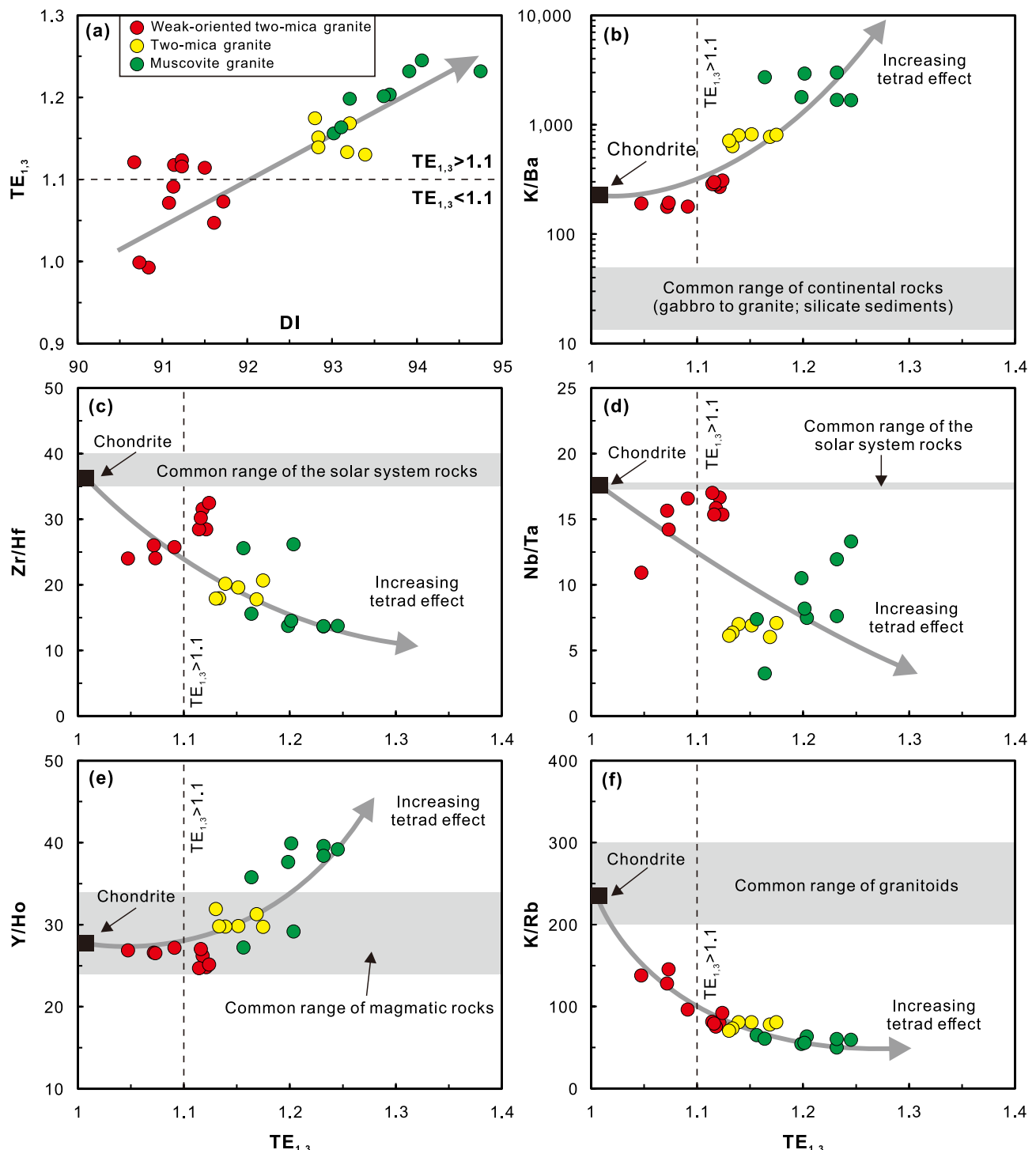


Fig. 16. (a) Differentiation index (DI), (b) K/Ba, (c) Zr/Hf, (d) Nb/Ta, (e) Y/Ho and (f) K/Rb vs. $TE_{1,3}$ plots for the Cuonadong leucogranites. $TE_{1,3}$ values are calculated based on formula proposed by Irber (1999).

(Fig. 15a and b). A previous study has revealed that tin deposits are genetically related to neighbouring tin-rich granites that contain tin in amounts >15 ppm (Lehmann and Harmanto, 1990). The Cuonadong leucogranites gradually evolved to tin-rich granite from the weakly-oriented two-mica granite to the muscovite granite (Fig. 15b). Huang and Jiang (2013) proposed that the Ba/Rb and Rb/Zr mass ratios can effectively distinguish W-rich (typically Ba/Rb mass ratio < 0.6 and Rb/Zr mass ratio > 6) and W-poor granite. According to this discrimination criterion, a part of weakly-oriented two-mica granite samples and all the two-mica granite and muscovite granite samples show features of W-rich granite (Fig. 15c, d). Therefore, although the primitive magma for the Cuonadong leucogranites was probably infertile due to low Sn, W and Be contents, the highly evolved magma could be very fertile after intense fractional crystallization.

Normally, crustal melts are viscous (Rutter et al., 2011), thus hard to differentiate. However, addition of volatiles (e.g., H₂O, F and B) can significantly reduce melt viscosity (e.g., Dingwell et al., 1996), which promotes an increase in the diffusivity of ionic components through the melt. In addition, B and F can markedly enhance the isobaric-isothermal solubility of H₂O in melt (London, 2009). The additional H₂O can further lower viscosity, and more importantly, forestalls the exsolution of a separate aqueous solution. Furthermore, volatiles can greatly extend the duration of fractional crystallization through significant reduction of magma solidus temperature (Manning, 1981), which sharply extend the enrichment duration for rare-metal elements. Obviously, presence of tourmaline-bearing leucogranite, pegmatite, hydrothermal vein and fluorite-rich greisen, skarn, and hydrothermal vein in or near the Cuonadong leucogranites suggest that the Cuonadong leucogranites were derived from a boron- and fluorine-rich magmatic system (Dai et al., 2019, 2022; Zhou et al., 2019; Cao et al., 2021b). Studies have revealed that the fluid-melt interaction in magmatic-hydrothermal system will result in an M-type REE tetrad effect in the melt and a W-type REE tetrad effect in the fluid (Scaillet et al., 1996; Zhao et al., 2002). Therefore, the increasing REE tetrad effect from the weakly-oriented two-mica granite to the two-mica granite and muscovite granite (Fig. 16a) suggests a gradually-enhanced fluid-melt interaction. Normally, twin elements, such as K-Rb, Nb-Ta and Zr-Hf have similar charge and radius and, therefore, yield chondritic ratios (CHARAC behavior) in magmatic systems (Jahn et al., 2001; Stepanov and Hermann, 2013). In contrast, in an aqueous system, twin-element pairs are typically characterized by non-CHARAC behavior (Bau, 1996) and have ratios different from the chondritic values (Jahn et al., 2001; Jiang et al., 2016; Yang et al., 2018). The twin-element pair ratios of the Cuonadong leucogranites deviate dramatically from the chondritic values, indicating an intense interaction between the residual melts and F-rich aqueous hydrothermal fluids (Fig. 16b-f; Jahn et al., 2001). Moreover, gradually obvious deviation is indicative of increasingly intense fluid-melt interaction. Therefore, the Cuonadong leucogranites were derived from a B, F and H₂O-rich magma system. Significantly, abundant volatiles not only guaranteed the occurrence of intensive and intense fractional crystallization through reduction of magma viscosity, but also extended duration of the fractional crystallization process (~21–15 Ma). These processes should have greatly facilitated enrichment of rare-metal elements in the residual magma, which is crucial for final rare-metal mineralization.

Thus, although Cuonadong leucogranites were derived from muscovite-induced partial melting of metapelites, partial melting was less likely the major process for rare-metal enrichment. In contrast, volatile-caused long-lasting (21–15 Ma) fractional crystallization was likely the main mechanism for rare-metal enrichment in the magma. In addition, the long duration (18–14 Ma) of rare-metal mineralization was likely responsible for the supernormal enrichment of Sn, W, and Be in the Cuonadong Sn-W-Be polymetallic deposit.

6. Conclusions

- (1) Major magmatism in the Cuonadong dome occurred during 21–15 Ma, while the rare-metal mineralization in the Cuonadong Sn-W-Be polymetallic deposit mainly occurred during 18–14 Ma.
- (2) The Cuonadong leucogranites are peraluminous S-type granites and were mainly derived from metapelites of the Higher Himalayan Crystalline Sequence.
- (3) The primitive magma for the Cuonadong leucogranites experienced gradually enhanced fractional crystallization and successively generated weakly-oriented two-mica granite, two-mica granite and muscovite granite.
- (4) The residual magma in Cuonadong became more and more enriched in rare-metal elements with continuous fractional crystallization, which made vital preparation of ore-forming metals for subsequent rare-metal mineralization.
- (5) The long-lived (21–15 Ma) fractional crystallization and long-lasting (18–14 Ma) rare-metal mineralization were collectively responsible for the supernormal enrichment of Sn, W, and Be in the Cuonadong Sn-W-Be polymetallic deposit.

Declaration of Competing Interest

The authors declare that they have no known competing financial interests or personal relationships that could have appeared to influence the work reported in this paper.

Data availability

Data will be made available on request.

Acknowledgments

This study was financially supported by the National Natural Science Foundation of China (grant/award numbers: 91955208, 92155305 and 42103066) and the China Geological Survey (grant/award number: DD20230008).

Appendix A. Supplementary data

Supplementary data to this article can be found online at <https://doi.org/10.1016/j.oregeorev.2023.105434>.

References

- Bau, M., 1996. Controls on the fractionation of isovalent trace elements in magmatic and aqueous systems: evidence from Y/Ho, Zr/Hf, and lanthanide tetrad effect. *Contrib. Miner. Petrol.* 123 (3), 323–333.
- Bonin, B., 2007. A-type granites and related rocks: evolution of a concept, problems and prospects. *Lithos* 97 (1), 1–29.
- Cao, H.W., Huang, Y., Li, G.M., Zhang, L.K., Wu, J.Y., Dong, L., Dai, Z.W., Lu, L., 2018. Late Triassic sedimentary records in the northern Tethyan Himalaya: tectonic link with Greater India. *Geosci. Front.* 9 (1), 273–291.
- Cao, H.W., Li, G.M., Zhang, Z., Zhang, L.K., Dong, S.L., Xia, X.B., Liang, W., Fu, J.G., Huang, Y., Xiang, A.P., Qing, C.S., Dai, Z.W., Pei, Q.M., Zhang, Y.H., 2020. Miocene Sn polymetallic mineralization in the Tethyan Himalaya, southeastern Tibet: a case study of the Cuonadong deposit. *Ore Geol. Rev.* 119 (1), 103403.
- Cao, H.W., Li, G.M., Zhang, L.K., Dong, L., Gao, K., Dai, Z.W., 2021a. Monazite U-Th-Pb age of Liemai Eocene granites in the southern Tibet and its geological implications. *Sediment. Geol. Tethyan Geol.* 40 (2), 31–42 in Chinese with English abstract.
- Cao, H.W., Li, G.M., Zhang, R.Q., Zhang, Y.H., Zhang, L.K., Dai, Z.W., Zhang, Z., Liang, W., Dong, S.L., Xia, X.B., 2021b. Genesis of the Cuonadong tin polymetallic deposit in the Tethyan Himalaya: Evidence from geology, geochronology, fluid inclusions and multiple isotopes. *Gondw. Res.* 92 (2), 72–101.
- Cao, H.W., Li, G.M., Zhang, L.K., Zhang, X.F., Yu, X., Chen, Y., Lin, B., Pei, Q.M., Tang, L., Zou, H., 2022a. Genesis of Himalayan leucogranite and its potentiality of rare-metal mineralization. *Sedimentary Geol. Tethyan Geol.* 42 (2), 189–211 in Chinese with English abstract.
- Cao, H.W., Pei, Q.M., Santosh, M., Li, G.M., Zhang, L.K., Zhang, X.F., Zhang, Y.H., Zou, H., Dai, Z.W., Lin, B., Tang, L., Yu, X., 2022b. Himalayan leucogranites: A review of geochemical and isotopic characteristics, timing of formation, genesis, and rare metal mineralization. *Earth Sci. Rev.* 234.

- Cao, K., Yang, Z.M., John, M., White, N.C., Xu, J.F., Li, Y., Li, W.K., 2019. Geology and Genesis of the Giant Pulang Porphyry Cu-Au District, Yunnan, Southwest China. *Econ. Geol.* 114 (2), 275–301.
- Chappell, B.W., 1999. Aluminium saturation in I- and S-type granites and the characterization of fractionated haplogranites. *Lithos* 46 (3), 535–551.
- Chappell, B.W., Simpson, P.R., 1984. Source rocks of I- and S-type granites in the Lachlan Fold Belt. *Southeastern Aust. Philos. Trans. R. Soc. London A: Math. Phys. Eng. Sci.* 310 (1514), 693–707.
- Chappell, B.W., White, A.J.R., 1992. I- and S-type granites in the Lachlan Fold Belt. *Earth Environ. Sci. Trans. R. Soc. Edinb.* 83 (1–2), 1–26.
- Chen, J.L., Xu, J.F., Yu, H.X., Wang, B.D., Wu, J.B., Feng, Y.X., 2015. Late Cretaceous high-Mg# granitoids in southern Tibet: Implications for the early crustal thickening and tectonic evolution of the Tibetan Plateau? *Lithos* 232, 12–22.
- Chen, X., Zhang, G.Y., Gao, R., Zhang, D.C., Yang, B., 2021. Petrogenesis of highly fractionated leucogranite in the Himalayas: The Early Miocene Cuonadong example. *Geol. J.* 56 (7).
- Chiaradia, M., Schaltegger, U., Spikings, R., Wotzlaw, J.F., Ovtcharova, M., 2013. How Accurately Can We Date the Duration of Magmatic-Hydrothermal Events in Porphyry Systems?—An Invited Paper. *Econ. Geol.* 108 (4), 565–584.
- Dai, Z.W., Li, G.M., Ding, J., Zhang, L.K., Cao, H.W., Zhang, Z., Liang, W., 2019. Chemical and boron isotopic composition, and significance of tourmaline from the Cuonadong tourmaline granite, Tibet. *Earth Sci.* 44 (6), 1849–1859 in Chinese with English abstract.
- Dai, Z.W., Dong, L., Li, G.M., Huizenga, J.M., Ding, J., Zhang, L.K., Huang, Y., Cao, H.W., Lu, L., Yan, G.Q., 2020. Crustal thickening prior to 43 Ma in the Himalaya: Evidence from lower crust-derived adakitic magmatism in Dala, eastern Tethyan Himalaya. *Tibet. Geol. J.* 55 (5), 4021–4046.
- Dai, Z.W., Li, G.M., Xie, Y.L., Yang, Z.M., Huizenga, J.M., Liang, W., Fu, J.G., Cao, H.W., 2022. Source and evolution of the ore-forming fluid of the Cuonadong Sn-W-Be polymetallic deposit (southern Tibet, China): constraints from scheelite trace element and Sr isotope geochemistry. *Ore Geol. Rev.* 104570.
- Dingwell, D.B., Pichavant, M., Holtz, F., 1996. Experimental studies of boron in granitic melts. *Rev. Mineral. Geochem.* 33 (1), 330–385.
- Eby, G.N., 1990. The A-type granitoids: A review of their occurrence and chemical characteristics and speculations on their petrogenesis. *Lithos* 26 (1–2), 115–134.
- Evensen, J.M., London, D., 2003. Experimental partitioning of Be, Cs, and other trace elements between cordierite and felsic melt, and the chemical signature of S-type granite. *Contrib. Miner. Petrol.* 144 (6), 739–757.
- Fei, G.C., Menuge, J.F., Li, Y.Q., Yang, J.Y., Deng, Y., Chen, C.S., Yang, Y.F., Yang, Z., Qin, L.Y., Zheng, L., Tang, W.C., 2020. Petrogenesis of the Lijiaogou spodumene pegmatites in Songpan-Garze Fold Belt, West Sichuan, China: Evidence from geochemistry, zircon, cassiterite and columbite U-Pb geochronology and Hf isotopic compositions. *Lithos* 364–365.
- Frost, B.R., Barnes, C.G., Collins, W.J., Arculus, R.J., Ellis, D.J., Frost, C.D., 2001. A Geochemical Classification for Granitic Rocks. *J. Petrol.* 42 (11), 2033–2048.
- Fu, J.G., Li, G.M., Wang, G.H., Huang, Y., Zhang, L.K., Dong, S.L., Liang, W., 2017. First field identification of the Cuonadong dome in southern Tibet: implications for EW extension of the North Himalayan gneiss dome. *Int. J. Earth Sci.* 106 (5), 1581–1596.
- Fu, J.G., Li, G.M., Wang, G.H., Zhang, L.K., Liang, W., Zhang, X.Q., Jiao, Y.J., Dong, S.L., Huang, Y., 2020. Structural analysis of sheath folds and geochronology in the Cuonadong Dome, southern Tibet, China: New constraints on the timing of the South Tibetan Detachment System and its relationship to North Himalayan Gneiss Domes. *Terra Nova* 32 (4), 300–323.
- Gao, L.E., Zeng, L.S., Asimow, P.D., 2017. Contrasting geochemical signatures of fluid-absent versus fluid-fluxed melting of muscovite in metasedimentary sources: The Himalayan leucogranites. *Geology* 45, 39–42.
- Gardien, V., Thompson, A.B., Grujic, D., Ulmer, P., 1995. Experimental melting of biotite + plagioclase+ quartz±muscovite assemblages and implications for crustal melting. *J. Geophys. Res.: Solid Earth* 100 (B8), 15581–15591.
- Glazner, A.F., Bartley, J.M., Coleman, D.S., Gray, W., Taylor, R.Z., 2004. Are plutons assembled over millions of years by amalgamation from small magma chambers? *GSA Today* 14 (4).
- Gou, Z.B., Zhang, Z.M., Dong, X., Xiang, H., Ding, H.X., Tian, Z.L., Lei, H.C., 2016. Petrogenesis and tectonic implications of the Yadong leucogranites, southern Himalaya. *Lithos* 256–257, 300–310.
- Gou, Z.B., Dong, X., Wang, B.D., 2019. Petrogenesis and Tectonic Implications of the Paiku Leucogranites, Northern Himalaya. *J. Earth Sci.* 30 (3), 525–534.
- Harris, N., Massey, J., 1994. Decompression and anatexis of Himalayan metapelites. *Tectonics* 13 (6), 1537–1546.
- He, C.T., Qin, K.Z., Zhao, J.X., Evans, N.J., Li, J.X., Zhou, Q.F., Li, G.M., 2022. Multiple skarn generations related to composite leucogranites in the Cuonadong Sn-W-Be deposit, Himalaya. *Ore Geol. Rev.* 150.
- Hopkinson, T.N., Harris, N.B.W., Warren, C.J., Spencer, C.J., Roberts, N.M.W., Horstwood, M.S.A., Parrish, R.R. and Eimf, 2017. The identification and significance of pure sediment-derived granites. *Earth and Planetary Science Letters*, 467: 57–63.
- Hou, Z.Q., Zheng, Y.C., Zeng, L.S., Gao, L.E., Huang, K.X., Li, W., Li, Q.Y., Fu, Q., Liang, W., Sun, Q.Z., 2012. Eocene-Oligocene granitoids in southern Tibet: Constraints on crustal anatexis and tectonic evolution of the Himalayan orogen. *Earth Planet. Sci. Lett.* 349–350, 38–52.
- Huang, C.M., Li, G.M., Zhang, Z., Liang, W., Huang, Y., Zhang, L.K. and Fu, J.G., 2018. Petrogenesis of the Cuonadong leucogranite in South Tibet: constraints from bulk-rock geochemistry and zircon U-Pb dating. *Earth Science Frontiers*, 25(6): 182–195 (in Chinese with English abstract).
- Huang, Y., Fu, J.G., Li, G.M., Zhang, L.K., Liu, H., 2019. Determination of Lalong dome in south Tibet and new discovery of rare metal mineralization. *Earth Sci.* 44 (7), 2197–2206 in Chinese with English abstract.
- Huang, L.C., Jiang, S.Y., 2013. Geochronology, geochemistry and petrogenesis of the tungsten-bearing porphyritic granite in the Dahutang tungsten deposit, Jiangxi Province. *Acta Petrol. Sin.* 29 (12), 4323–4335 in Chinese with English abstract.
- Huang, C.M., 2019. Petrogenesis of the Cuonadong-Lhoga leucogranites and implication for tectonic evolution and Be-W-Sn metallogenesis in southern Tibet. Doctoral Degree Thesis, China University of Geosciences (Beijing), (in Chinese with English abstract) pp.
- Irber, W., 1999. The lanthanide tetrad effect and its correlation with K/Rb, Eu/Eu*, Sr/Eu, Y/Ho, and Zr/Hf of evolving peraluminous granite suites. *Geochim. Cosmochim. Acta* 63 (3), 489–508.
- Jahn, B.-M., Wu, F.Y., Capdevila, R., Martineau, F., Zhao, Z.H., Wang, Y.X., 2001. Highly evolved juvenile granites with tetrad REE patterns: the Woduhe and Baerzhe granites from the Great Xing'an Mountains in NE China. *Lithos* 59 (4), 171–198.
- Jiang, S.H., Bagas, L., Hu, P., Han, N., Chen, C.L., Liu, Y., Kang, H., 2016. Zircon U-Pb ages and Sr-Nd-Hf isotopes of the highly fractionated granite with tetrad REE patterns in the Shamai tungsten deposit in eastern Inner Mongolia: Implications for the timing of mineralization and ore genesis. *Lithos* 261, 322–339.
- Karakas, O., Degruyter, W., Bachmann, O., Dufek, J., 2017. Lifetime and size of shallow magma bodies controlled by crustal-scale magmatism. *Nat. Geosci.* 10 (6), 446–450.
- Kohn, M.J., 2014. Himalayan Metamorphism and Its Tectonic Implications. *Annu. Rev. Earth Planet. Sci.* 42 (1), 381–419.
- Kunz, B.E., Warren, C.J., Jenner, F.E., Harris, N.B.W., Argles, T.W., 2022. Critical metal enrichment in crustal melts: The role of metamorphic mica. *Geology*.
- Le Fort, P., Cuney, M., Deniel, C., France Lanord, C., Sheppard, S.M.F., Upreti, B.N., Vidal, P., 1987. Crustal generation of the Himalayan leucogranites. *Tectonophysics* 134 (1), 39–57.
- Lee, J.-Y., Marti, K., Severinghaus, J.P., Kawamura, K., Yoo, H.-S., Lee, J.B., Kim, J.S., 2006. A redetermination of the isotopic abundances of atmospheric Ar. *Geochim. Cosmochim. Acta* 70 (17), 4507–4512.
- Lee, C.-T.A., Morton, D.M., 2015. High silica granites: Terminal porosity and crystal settling in shallow magma chambers. *Earth Planet. Sci. Lett.* 409, 23–31.
- Lehmann, B., 1990. Metallogeny of Tin. Springer-Verlag, Berlin Heidelberg.
- Lehmann, B. and Harmanto, 1990. Large-scale tin depletion in the Tanjungpandan tin granite, Belitung Island, Indonesia. *Economic Geology*, 85(1): 99–111.
- Li, G.M., Fu, J.G., Guo, W.K., Zhang, H., Zhang, L.K., Dong, S.L., Li, Y.X., Wu, J.Y., Jiao, Y.J., Jin, C.H., Huang, C.M., 2022. Discovery of the Gabo granitic pegmatite-type lithium deposit in the Kulangangri Dome, eastern Himalayan metallogenic belt, and its prospecting implication. *Acta Petrol. Mineral.* 41 (6), 1109–1119 in Chinese with English abstract.
- Li, Y., Li, X.H., Selby, D., Li, J.W., 2017b. Pulsed magmatic fluid release for the formation of porphyry deposits: Tracing fluid evolution in absolute time from the Tibetan Qulong Cu-Mo deposit. *Geology*.
- Li, H., Myint, A.Z., Yonezu, K., Watanabe, K., Algeo, T.J., Wu, J.-H., 2018. Geochemistry and U-Pb geochronology of the Wagone and Hermyingyi A-type granites, southern Myanmar: Implications for tectonic setting, magma evolution and Sn-W mineralization. *Ore Geol. Rev.* 95, 575–592.
- Li, G.M., Zhang, L.K., Jiao, Y.J., Xia, X.B., Dong, S.L., Fu, J.G., Liang, W., Zhang, Z., Wu, J.Y., Dong, L., Huang, Y., 2017a. First discovery and implications of Cuonadong superlarge Be-W-Sn polymetallic deposit in Himalayan metallogenic belt, southern Tibet. *Mineral Deposits* 36 (4), 1003–1008 in Chinese with English abstract.
- Liang, W., Zhang, L.K., Xia, X.B., Ma, G.T., Huang, Y., Zhang, Z., Fu, J.G., Cao, H.W., Miao, H.Q., Li, G.M., 2018. Geology and preliminary mineral genesis of the Cuonadong W-Sn polymetallic deposit, southern Tibet, China. *Earth Sci.* 43 (8), 2742–2754 in Chinese with English abstract.
- Lin, B., Tang, J.X., Zheng, W.B., Leng, Q.F., Lin, X., Wang, Y.Y., Meng, Z., Tang, P., Ding, S., Xu, Y.F., 2016a. Geochemical characteristics, age and genesis of Cuonadong leucogranite, Tibet. *Acta Petrologica et Mineralogica* 35 (3), 391–406 in Chinese with English abstract.
- Lin, B., Tang, J.X., Zheng, W.B., Leng, Q.F., Lin, X., Wang, Y.Y., Meng, Z., Tang, P., Ding, S., Xu, Y.F., 2016b. Geochemical characteristics, age and genesis of Cuonadong leucogranite, Tibet. *Acta Petrologica Et Mineralogica* 35 (3), 391–406 in Chinese with English abstract.
- London, D., 2009. The Origin of Primary Textures in Granitic Pegmatites. *Can. Mineral.* 47 (4), 697–724.
- Maniar, P.D. and Piccoli, P.M., 1989. Tectonic discrimination of granitoids. *Geological Society of America Bulletin*, 101(5): 635–643.
- Manning, D.A.C., 1981. The effect of fluorine on liquidus phase relationships in the system Qz-Ab-Or with excess water at 1 kb. *Contrib. Miner. Petrol.* 76 (2), 206–215.
- Mo, X.X., Zhao, Z.D., Zhou, S., Dong, G.C., Liao, Z.L., 2007. On the timing of India-Asia continental collision. *Geol. Bull. China* 26 (10), 1240–1244 in Chinese with English abstract.
- Mukherjee, P.K., Jain, A.K., Singhal, S., Singha, N.B., Singh, S., Kumud, K., Seth, P., Patel, R.C., 2019. U-Pb zircon ages and Sm-Nd isotopic characteristics of the Lesser and Great Himalayan sequences, Uttarakhand Himalaya, and their regional tectonic implications. *Gondw. Res.* 75, 282–297.
- Myrow, P.M., Fike, D.A., Malmkog, E., Leslie, S.A., Zhang, T., Singh, B.P., Chaubey, R.S., Prasad, S.K., 2019. Ordovician–Silurian boundary strata of the Indian Himalaya: Record of the latest Ordovician Boda event. *Geol. Soc. Am. Bull.* 131 (5–6), 881–898.
- Pan, G.T., Xiao, Q.H., Lu, S.N., Den, J.F., Feng, Y.M., Zhang, K.X., Zhang, Z.Y., Wang, F.G., Xing, G.F., Hao, G.J., Feng, Y.F., 2009. Subdivision of tectonic units in China. *Geol. China* 36 (1), 1–28 in Chinese with English abstract.
- Pan, G.T., Wang, L.Q., Li, R.S., Yuan, S.H., Ji, W.H., Yin, F.G., Zhang, W.P., Wang, B.D., 2012. Tectonic evolution of the Qinghai-Tibet Plateau. *J. Asian Earth Sci.* 53, 3–14.
- Patino Douce, A.E., 1999. What do experiments tell us about the relative contributions of crust and mantle to the origin of granitic magmas? *Geol. Soc. Lond. Spec. Publ.* 168 (1), 55–75.

- Patiño-Douce, A.E., Harris, N., 1998. Experimental Constraints on Himalayan Anatexis. *J. Petrol.* 39 (4), 689–710.
- Petford, N., Cruden, A.R., McCaffrey, K.J.W., Vigneresse, J.L., 2000. Granite magma formation, transport and emplacement in the Earth's crust. *Nature* 408, 669–673.
- Qin, K.Z., Zhao, J.X., He, C.T., Shi, R.Z., 2021. Discovery of the Qongjiagang giant lithium pegmatite deposit in Himalaya Tibet, China. *Acta Petrologica Sinica* 37 (11), 3277–3286 in Chinese with English abstract.
- Rollinson, H.R., 1993. Using geochemical data: evaluation, presentation, interpretation. Routledge.
- Romer, R.L., Pichavant, M., 2021. Rare Metal Granites and Pegmatites. *Encyclopedia Geol.* 840–846.
- Rudnick, R.L., Gao, S., 2003. Composition of the Continental Crust. In: Turekian, K.K. (Ed.), *Treatise on Geochemistry*. Pergamon, Oxford, pp. 1–64.
- Rutter, E.H., Mecklenburgh, J., Brodie, K.H., 2011. Rock mechanics constraints on mid-crustal low-viscosity flow beneath Tibet. *Geol. Soc. Lond. Spec. Publ.* 360 (1), 329–336.
- Scaillet, B., Holtz, F., Pichavant, M., Schmidt, M., 1996. Viscosity of Himalayan leucogranites: Implications for mechanisms of granitic magma ascent. *J. Geophys. Res. Solid Earth* 101 (B12), 27691–27699.
- Simons, B., Andersen, J.C.Ø., Shail, R.K., Jenner, F.E., 2017. Fractionation of Li, Be, Ga, Nb, Ta, In, Sn, Sb, W and Bi in the peraluminous Early Permian Variscan granites of the Cornubian Batholith: Precursor processes to magmatic-hydrothermal mineralisation. *Lithos* 278–281, 491–512.
- Stepanov, A.S., Hermann, J., 2013. Fractionation of Nb and Ta by biotite and phengite: Implications for the “missing Nb paradox”. *Geology* 41 (3), 303–306.
- Stepanov, A.S., Hermann, J., Rubatto, D., Rapp, R.P., 2012. Experimental study of monazite/melt partitioning with implications for the REE, Th and U geochemistry of crustal rocks. *Chem. Geol.* 300–301, 200–220.
- Sun, S.S., McDonough, W.F., 1989. Chemical and isotopic systematics of oceanic basalts: implications for mantle composition and processes. *Geol. Soc. Lond. Spec. Publ.* 42 (1), 313–345.
- Sylvester, P.J., 1998. Post-collisional strongly peraluminous granites. *Lithos* 45 (1–4), 29–44.
- Wang, X.X., Zhang, J.J., Yan, S.Y., Liu, J., Wang, J.M. and Guo, L., 2015. Age and formation mechanism of the Qiamangba two-mica granite in northern Himalaya. *Chinese Journal of Geology*, 50: 708–727(in Chinese with English abstract).
- Wang, R.C., Wu, F.Y., Xie, L., Liu, X.C., Wang, J.M., Yang, L., Lai, W., Liu, C., 2017. A preliminary study of rare-metal mineralization in the Himalayan leucogranite belts, South Tibet. *Sci. China Earth Sci.* 60 (9), 1655–1663.
- Whalen, J.B., Currie, K.L., Chappell, B.W., 1987. A-type granites: geochemical characteristics, discrimination and petrogenesis. *Contrib. Miner. Petrol.* 95 (4), 407–419.
- Wu, F.Y., Liu, Z.C., Liu, X.C., Ji, W.Q., 2015. Himalayan leucogranite: Petrogenesis and implications to orogenesis and plateau uplift. *Acta Petrol. Sin.* 31 (1), 1–36 in Chinese with English abstract.
- Wu, F.Y., Liu, X.C., Liu, Z.C., Wang, R.C., Xie, L., Wang, J.M., Ji, W.Q., Yang, L., Liu, C., Khanal, G.P., He, S.X., 2020. Highly fractionated Himalayan leucogranites and associated rare-metal mineralization. *Lithos* 352–353, 105319.
- Xie, Y.L., Li, L.M., Wang, B.G., Li, G.M., Liu, H.F., Li, Y.X., Dong, S.L., Zhou, J.J., 2017. Genesis of the Zhaxikang epithermal Pb-Zn-Sb deposit in southern Tibet, China: Evidence for a magmatic link. *Ore Geol. Rev.* 80, 891–909.
- Xie, L., Tao, X.Y., Wang, R.C., Wu, F.Y., Liu, C., Liu, X.C., Li, X.K., Zhang, R.Q., 2020. Highly fractionated leucogranites in the eastern Himalayan Cuonadong dome and related magmatic Be-Nb-Ta and hydrothermal Be-W-Sn mineralization. *Lithos* 354–355 (7), 105286.
- Xu, B., Hou, Z.-Q., Zheng, Y.-C., Wang, R., He, M.-Y., Zhou, L.-M., Wang, Z.-X., He, W.-Y., Zhou, Y., Yang, Y., 2017. In situ elemental and isotopic study of diorite intrusions: implication for Jurassic arc magmatism and porphyry Cu-Au mineralization in southern Tibet. *Ore Geol. Rev.* 90, 1063–1077.
- Yan, Q.-H., Wang, H., Chi, G., 2020. Pulsed magmatic fluid releasing in the formation of the Taoxihu Sn polymetallic deposit, eastern Guangdong, SE China: Evidence from fluid inclusions, cassiterite U-Pb geochronology, and stable isotopes. *Ore Geol. Rev.* 126, 103724.
- Yang, Z.Y., Wang, Q., Zhang, C.F., Dan, W., Zhang, X.Z., Qi, Y., Xia, X.P., Zhao, Z.H., 2018. Rare earth element tetrad effect and negative Ce anomalies of the granite porphyries in southern Qiangtang Terrane, central Tibet: New insights into the genesis of highly evolved granites. *Lithos* 312–313, 258–273.
- Yin, A., 2006. Cenozoic tectonic evolution of the Himalayan orogen as constrained by along-strike variation of structural geometry, exhumation history, and foreland sedimentation. *Earth Sci. Rev.* 76 (1–2), 1–131.
- Yin, A., Harrison, T.M., 2000. Geologic evolution of the Himalayan-Tibetan orogen. *Annu. Rev. Earth Planet. Sci.* 28 (1), 211–280.
- Zeng, L.S., Gao, L.E., Xie, K.J., Jing, L.Z., 2011. Mid-Eocene high Sr/Y granites in the Northern Himalayan Gneiss Domes: Melting thickened lower continental crust. *Earth Planet. Sci. Lett.* 303, 251–266.
- Zhang, Z.Y., Hou, Z.Q., Peng, H.M., Fan, X.K., Wu, X.Y., Dai, J.L., 2019c. In situ oxygen isotope, trace element, and fluid inclusion evidence for a primary magmatic fluid origin for the shell-shaped pegmatoid zone within the giant Dahutang tungsten deposit, Jiangxi Province, South China. *Ore Geol. Rev.* 104, 540–560.
- Zhang, L.K., Li, G.M., Santos, M., Cao, H.W., Dong, S.L., Zhang, Z., Fu, J.G., Xia, X.B., Huang, Y., Liang, W., Zhang, S.T., 2019a. Cambrian magmatism in the Tethys Himalaya and implications for the evolution of the Proto-Tethys along the northern Gondwana margin: A case study and overview. *Geol. J.* 54 (4), 2545–2565.
- Zhang, L.K., Li, G.M., Cao, H.W., Zhang, Z., Dong, S.L., Liang, W., Fu, J.G., Huang, Y., Xia, X.B., Dai, Z.W., Pei, Q.M., Zhang, S.T., 2020. Activity of the south Tibetan detachment system: Constraints from leucogranite ages in the eastern Himalayas. *Geol. J.* 55 (7), 5540–5573.
- Zhang, Z., Li, G.M., Zhang, L.K., Cao, H.W., Yang, C., Huang, Y., Liang, W., Fu, J.G., Dong, S.L., Xia, X.B., Dai, Z.W., 2021. Neoproterozoic bimodal magmatism in the eastern Himalayan orogen: Tectonic implications for the Rodinia supercontinent evolution. *Gondw. Res.* 94, 87–105.
- Zhang, Z., Li, G.M., Zhang, L.K., 2022. Exploration and research progresses of rare metals in Himalayan belt, Tibet. *Sedimentary Geol. Tethyan Geol.* 42 (2), 176–188 in Chinese with English abstract.
- Zhang, J.J., Santos, M., Wang, X.X., Guo, L., Yang, X.Y., Zhang, B., 2012. Tectonics of the northern Himalaya since the India-Asia collision. *Gondw. Res.* 21, 939–960.
- Zhang, L.X., Wang, Q., Zhu, D.C., Li, S.M., Zhao, Z.D., Zhang, L.L., Chen, Y., Liu, S.A., Zheng, Y.C., Wang, R., Liao, Z.L., 2019b. Generation of leucogranites via fractional crystallization: A case from the Late Triassic Luoza batholith in the Lhasa Terrane, southern Tibet. *Gondw. Res.* 66, 63–76.
- Zhao, Z., Liu, C., Guo, N.-X., Zhao, W.W., Wang, P.-A., Chen, Z.-H., 2018. Temporal and spatial relationships of granitic magmatism and W mineralization: Insights from the Xingguo orefield, South China. *Ore Geol. Rev.* 95, 945–973.
- Zhao, Z.H., Xiong, X.L., Han, X.D., Wang, Y.X., Wang, Q., Bao, Z.W., Jahn, B., 2002. Controls on the REE tetrad effect in granites: Evidence from the Qianlshan and Baerzhe Granites, China. *Geochem. J.* 36 (6), 527–543.
- Zhou, Q., Li, W.C., Wang, G.C., Liu, Z., Lai, Y., Huang, J.H., Yan, G.Q., Zhang, Q.C., 2019. Chemical and boron isotopic composition of tourmaline from the Conadong leucogranite-pegmatite system in South Tibet. *Lithos* 326–327, 529–539.
- Zhu, D.C., Wang, Q., Zhao, Z.D., Chung, S.L., Cawood, P.A., Niu, Y.L., Liu, S.A., Wu, F.Y., Mo, X.X., 2015. Magmatic record of India-Asia collision. *Sci. Rep.* 5, 14289.